In: Nanostructures
Editor: Yu Dong
ISBN: 978-1-62618-081-9

Chapter 8

MECHANICAL PROPERTIES OF CONTINUOUS NANOFIBERS: CHARACTERIZATION AND MECHANICS

Xiang-Fa Wu*, Zhengping Zhou, Arifur Rahman and Amol Bedarkar
Department of Mechanical Engineering, North Dakota State University, Fargo, North Dakota, USA

ABSTRACT

Mechanical properties are fundamental to the potential structural and functional applications of continuous nanofibers produced by electrospinning. Due to their unique continuity, high specific surface area, tailorable material properties and microstructures, low cost in manufacturing and excellent scalability, electrospun nanofibers have found rapidly expanding applications in structural, biomedical and bioengineering, environmental, and renewal energy sectors, among others. This chapter focuses on the production, mechanical characterization and mechanics modeling of these continuous nanofibers.

A brief introduction to electrospinning and continuous nanofibers as well as scalable nanofiber manufacturing is given. Several cutting-edge experimental techniques for mechanical characterization of continuous nanofibers are reviewed. The unique mechanical responses of electrospun nanofibers are discussed including the size effect in mechanical characterization, failure mechanisms, surface instability, etc. In addition, several recently developed continuum mechanics models are presented to correlate the experimental observations of electrospun nanofibers such as the size effect in mechanical properties, wave propagation, surface rippling, adhesion and contact, surface wetting, hydroelastic response, etc. These mechanics models are expected to place the manufacturing, characterization and applications of continuous electrospun nanofibers on a rational foundation.

* Corresponding author's email address: Xiangfa.Wu@ndsu.edu.

INTRODUCTION

Nanomaterials or nanostructured materials are defined as materials or structures with at least one dimension in the size of nanoscale (<100 nm). The morphology of nanomaterials can be zero-dimensional (0D) such as nanoparticles, nanoclusters and quantum dots, one-dimensional (1D) such as carbon nanotubes (CNTs), silicon nanowires (SNWs), magnetic nanorods and continuous polymer nanofibers, two-dimensional (2D) such as biological membranes and graphene, and complicated three-dimensional (3D) nanostructures. Among these, each nanomaterial corresponds to one or several specifically developed nanofabrication techniques. For example, chemical vapor deposition (CVD) can be utilized for synthesis of CNTs and nanowires of silicon, metal and metal oxides; electric nanolithography can be used to produce well patterned nanostructures. Due to the unique size effect in their chemical and physical properties, nanomaterials are expected to provide promising properties that their counterpart bulk materials do not carry, including improved stiffness, strength, thermal and electrical conductivities, chemical activity, etc.

Among various nanomaterials, continuous nanofibers produced by electrospinning [1-7] represent a relatively new type of nanostructured materials. To date, hundreds of natural and synthetic polymers as well as polymer-derived metals, metal oxides, carbon, silicon, and ceramics have been successfully electrospun into nanofibers and nanowires with the diameters in the range of 1-2,000 nm [6, 8-13]. The broad spectrum of electrospinnable materials and relatively low fabrication cost of the electrospinning technique have attracted fast growing research and industrial interests in this field in the recent years. As evidenced, a rapidly increasing number of materials scientists, engineers and chemists in academic communities and industries have joined the intensive research and commercial development of electrospun nanofibers for various applications. These applications include filter media, nanocomposites, wound dressing, biomedicine and tissue engineering, sensors and transducers, renewable energy harvesting, conversion, and storage devices, etc. [7-17]. As a result, the number of publications and article citations relevant to electrospinning and electrospun nanofibers increases very fast since the first paper on modern electrospinning published by Doshi and Reneker in 1995 [1].Moreover, recent technological breakthroughs in the bottleneck of scalable mass production of continuous nanofibers such as use of the needleless electrospinning technique (e.g., the Nanospider™ of Elmarco Inc., Czech) have paved the path for industry-level applications of a large quantity of continuous electrospun nanofibers.

Yet, compared to the fast development of nanofiber fabrication and applications, the fundamental understanding of the mechanical properties of electrospun nanofibers and relevant mechanics models are still highly desired since the mechanical properties of electrospun nanofibers are fundamental to fulfilling their structural and functional applications. Therefore, in this chapter, we are going to discuss the production, mechanical characterization and mechanics modeling of continuous nanofibers. To do so, a brief introduction will be given on electrospinning technique, scalable nanofiber manufacturing, and simplified process modeling. Recently developed techniques for mechanical characterization of continuous nanofibers will be reviewed. Several unique mechanical responses of electrospun nanofibers will be addressed such as the size effect observed in the mechanical measurements, failure mechanisms, surface instability, etc. Moreover, to

understand the unique mechanical behavior of electrospun nanofibers such as the size effect in axial quasi-static mechanical behavior, wave propagation, surface rippling, adhesion and contact, surface wetting, hydroelastic response, etc., several continuum mechanics models developed recently by the authors and others will be presented. These phenomenological mechanics models can serve as the rational foundation useful to better manufacturing, mechanical characterization and applications of electrospun nanofibers in ever expanding research and industrial areas.

ELECTROSPINNING AND NANOFIBERS—TECHNOLOGICAL DEVELOPMENT AND CHALLENGES

Electrospinning is based on the principle of electrohydrodynamic jetting from a polymer solution or melt [1-5]. This technique has been broadly utilized for fabricating continuous nanofibers and nanowires of natural and synthetic polymers and polymer-derived carbon, ceramics, metals, metal oxides, etc. [7-17]. Schematic setup of conventional needle-based electrospinning is illustrated in figure 1, which is simply made up with an adjustable high-voltage direct current (DC) power supply, a capillary tube, and a conductive fiber collector (usually a metallic plate). During a typical electrospinning process, under the action of electrostatic force (onto the induced charges) on the polymer solution, a droplet forms from the capillary tube and deforms into a Taylor cone [18-20]. When the electrostatic force overcomes the surface tension, a charged thin jet is elongated and accelerated in the electrostatic field. After a variety of jet destabilizations and solvent evaporation (drying), the ultra-thinned jet is finally deposited on the fiber collector to form a nonwoven nanofiber mat. Figure 2 shows a few types of typical nanofibers produced by means of electrospinning technique in our recent research. To date, hundreds of synthetic and natural polymers have been produced by electrospinning [6, 8, 11, 12].

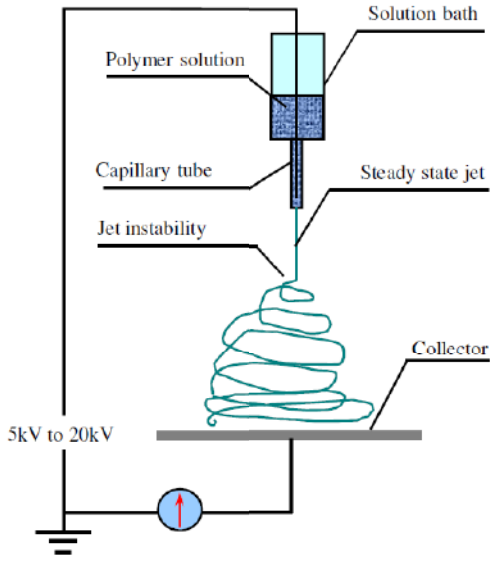

Figure 1. Schematic of electrospinning setup.

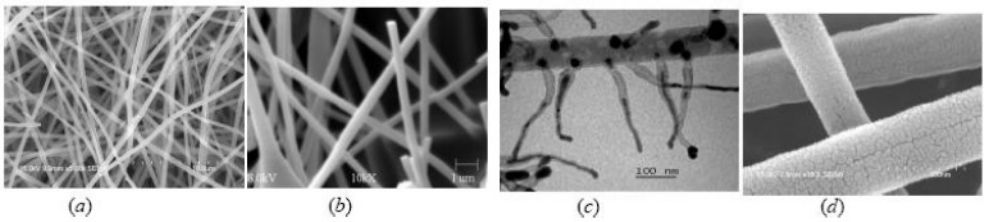

Figure 2. Continuous nanofibers produced by electrospinning: (*a*) polyimide (PI), (*b*) polyacrylonitrile (PAN)-based carbon, (*c*) carbon nanotube (CNT)-grafted carbon [21]. [Copyright (2008) of the Institute of Physics], and (*d*) nano-cracked chromium-coated nanofibers.

Continuous nanofibers collected in electrospinning can be in the form of highly porous nonwoven nanofiber mats or aligned nanofiber films with the aid of specially designed collectors or an auxiliary DC or alterative current (AC) electric field [22]. So far, electrospinning technique and electrospun nanofibers have become a worldwide topic of interest due to their rapidly expanding applications in protective clothing [23], filtration [8, 24-27], templates for synthesizing metallic and polymer nanotubes [8, 28, 29], precursors for fabricating carbon nanofibers [21, 30, 31], and nanofiber composites [32-34]. Furthermore, electrospun nanofibers have also been considered in biomedical engineering and technologies (e.g., medications [35,36], scaffolds for tissue growth [37-42], drug delivery systems [43-46], etc.), dye-sensitized solar cells [47-48], super-hydrophobic surfaces [49, 50], nanofiber sensors [51-55], etc. The near future applications of electrospun nanofibers may also include solar sails, light sails and mirrors in space and nanoelectronics [56], and porous nanofiber electrodes for rechargeable lithium ion batteries [57-59], among others.

Yet, the conventional single-nozzle based electrospinning technique has a very low productivity. One technical resolution of enhancing the nanofiber productivity triggered by the traditional fiber spinning technology is to utilize multiple spinnerets [60] as commercialized in several electrospinning machines in the market (e.g., eSpinner™). In principle, multi-spinneret based electrospinning can increase the nanofiber productivity in proportion to the number of spinnerets installed; however, severe technical barriers have been experienced such as spinneret clogging due to solvent evaporation near the outlets [3], among others.

Such technical disadvantages in the conventional needle-based electrospinning technique have challenged researchers all over the world to search for more robust and productive electrospinning techniques for continuous, scalable production of nanofibers. Among others, Yarin and Zussman [61] first proposed an experimental prototype of needleless electrospinning as shown in figure 3, in which dozens of jets can be generated simultaneously from a free surface of polymer solution. The seminal contribution of Yarin and Zussman's needleless electrospinning concept is to artificially induce the free-surface destabilization via employing an external magnetic field to a second magnetizable fluid underneath the polymer solution.

Along the vein of free-surface jetting, the research group at Technical University of Liberec in Czech Republic made a technical breakthrough in the needleless electrospinning technology by utilizing free-jetting of a thin-liquid layer formed on a rotating drum [62-65], as shown in figure 4. This technical innovation directly led to the birth of the Nanospider™, a robust and efficient needleless electrospinning device commercialized successfully by

Elmarco, Inc., the world's first and largest supplier of industrial scale nanofiber production machines.

In recent years, the Nanospider™ needleless electrospinning machines have been installed in over one hundred companies and universities in the U.S. for mass fabrication of continuous nanofibers of various natural and synthetic polymers. It needs to be mentioned that two key technological innovations have been fulfilled through the Nanospider™: (1) thickness of the thin-liquid layer can be tailored through adjusting the drum radius, rotating angular speed, or drum surface properties (e.g., surface roughness, hydrophobicity, etc.); (2) the thin-film thickness is maintained by the rotating drum that makes it possible for robust, mass production of continuous nanofibers. Based on the electrohydrodynamic principle of free jetting from a thin liquid film on a rotating drum as employed in the Nanospider™, new technical features are under further exploration such as mass production of core-shell nanofibers, etc.

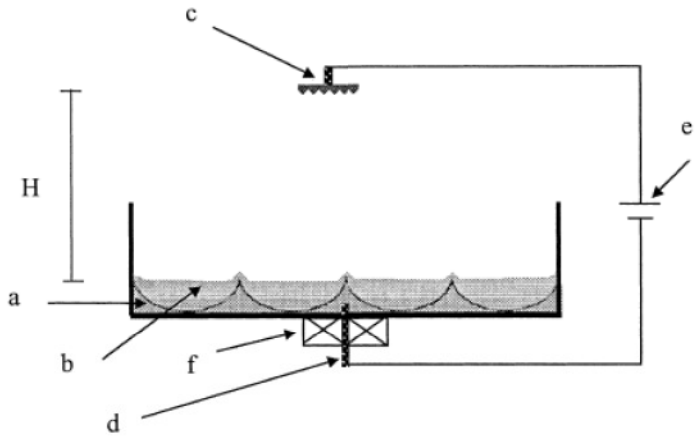

Figure 3. Schematic of the first needleless electrospinning setup proposed by Yarin and Zussman [61]: (*a*) a layer of magnetic liquid, (*b*) a layer of polymer solution, (*c*) counter-electrode located at a distance *H* from the free surface of the polymer solution, (*d*) electrode submerged into the magnetic fluid, (*e*) high voltage source, and (*f*) strong permanent magnet or electromagnet. Copyright (2004) of Elsevier.

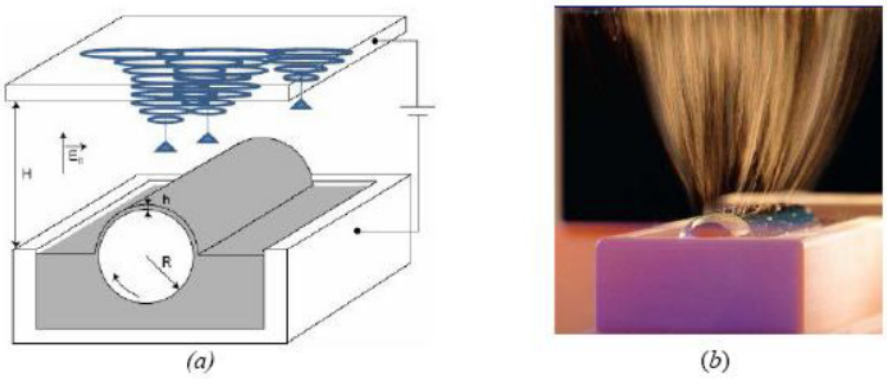

Figure 4. (*a*) Concept of free-surface jetting from thin liquid layer in a high DC electrostatic field [62-65]; (*b*) multiple jets from a rotating drum of a needleless electrospinning machine: Nanospider™ (Elmarco, Inc., Czech, 2010). Copyright (2008) of the American Institute of Physics.

Besides, recent technological development also considers spinning core-shell and hollow nanofibers by means of coelectrospinning [66-68] and emulsion electrospinning [69-72]. The coelectrospinning technique for core-shell nanofibers is based on a double-compartment syringe as shown in figure 5(*a*). During the process, two polymer solutions are supplied simultaneously to form a coaxial Taylor's cone. Upon destabilization of the coaxial Taylor cone in an electrostatic field, a coaxial jet can be formed, stretched, and accelerated underproper condition.

After solvent evaporation (drying), the whipping coaxial jet forms coaxial nanofibers as shown in figure 5(*b*). Compared to conventional single-nozzle based electrospinning, double numbers of material and geometrical parameters (coaxial nozzle) are involved in a coelectrospinning process, which provide more flexible options for controlled coaxial nanofiber fabrication. One superior advantage of the coelectrospinning technique is that it can spin unelectrospinnable materials such as small-molecule monomers, liquids, etc. Furthermore, Yarin and his collaborators [69] recently found that core-shell nanofibers can also be formed by using an emulsion electrospinning technique, which is based still on a conventional single-nozzle based electrospinning setup as shown in figure 6 [69-72]. In their demonstration, the electrospinnable PMMA/DMF and PAN/DMF solutions were first blended and then stored in room temperature without stirring for 12 hours. During this period, the blend decomposed into PMMA/DMF droplets with the diameter of ~100 μm in the PAN/DMF solution.

The resulting emulsion can be electrospun using a standard single-nozzle electrospinning setup (figure 1). During such an electrospinning process, the coaxial Taylor cone can be formed instantaneously at the moment when a PMMA/DMF droplet enters the nozzle exit [72]. Subsequently, the enwrapped PMMA/DMF droplets were deformed, stretched substantially, and finally form the core material after drying. A detailed review was made recently by Yarin [72] on the development of coelectrospinning and emulsion electrospinning techniques and related applications.

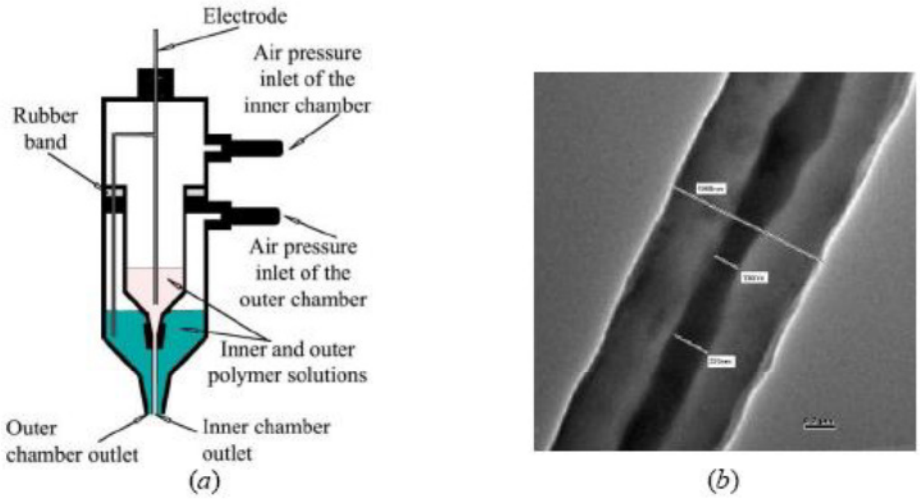

Figure 5. (*a*) Schematic of coelectrospinning setup[66] and (*b*) TEM micrograph of the core-shell structure of unstained samples of coelectrospun poly (ethylene oxide) (PEO, sheath) and poly (dodecylthiophene) (PDT, core) [66]. Copyright (2003) of the Wiley and Sons, Inc.

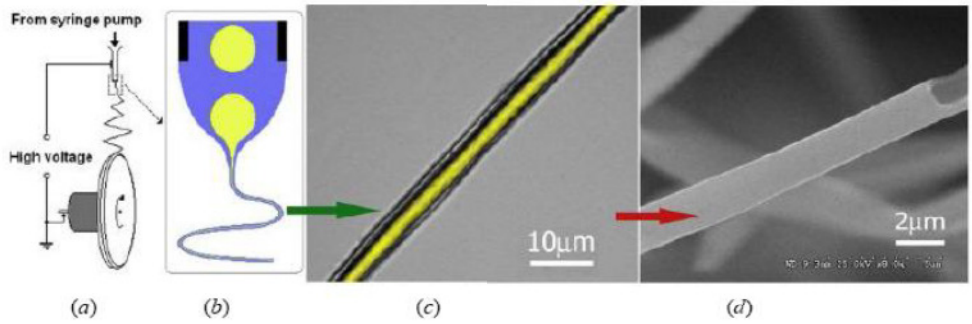

Figure 6. (*a*) Schematic setup of emulsion electrospinning of PMMA/PAN blend in DMF using a single circular nozzle; (*b*) schematic of magnified details of the needle orifice, in which the PMMA/DMF droplets are shown in yellow and the PAN/DMF liquid in blue, the liquids wet the nozzle, and the core-sheath fibers emanating from the Taylor's cone tip are collected on the edge of a rotating wheel; (*c*) SEM micrograph of core-shell fibers produced by this method; and (*d*) SEM micrograph of a hollow fiber obtained through elimination of the core material [69-72]. Copyright (2007) of the American Society of Chemistry.

Nevertheless, there is still lacking the fundamental understanding of the entire process of needleless electrospinning and coelectrospinning such as electrohydrodynamic multi-jet initiation and stretching, solvent evaporation (drying), porous structural formation, and controlled nanofiber collection though several preliminary models have been formulated that were essentially focused on understanding the electrohydrodynamic destabilization of thin liquid films and droplets [62, 73-85]. As a matter of fact, for mass fabrication of nanofibers, the current needleless electrospinning machine (e.g., the Nanospider^{TM}) typically needs a substantial period of empirical trial and error in determining the optimal process parameters for a specific polymer-solvent system. Such a process is laborious and usually carried out with the assistance of experienced experts from the machine manufacturers or through special on-site training. Thus, similar to other controllable fabrications, process modeling of electrospinning is extremely important to the fundamental understanding of the electrohydrodynamic phenomenon of electrospinning process and controllable fabrication of nanofibers for wider use of nanofibers.

PROCESS MODELING OF ELECTROSPINNING

As mentioned in the above, the experimental setup for either nozzle-based electrospinning (figure 1), recently developed needleless electrospinning (figure 3), or coelectrospinning (figure 5) is relatively simple and low cost; however the entire electrospinning process is an extremely complicated multi-physics phenomenon coupled with electrohydrodynamics, heat/mass diffusion and transfer, nonlinear rheology, polymer solidification, etc. For noozle-based electrospinning, several theoretical models have been proposed to treat specific one or two individual stages of the process: formation of Taylor cone [18-20], jet initiation, steadily accelerating straight jet, or jet whipping, etc., each of which involves the combined action of electrostatic force, capillary effect, non-newtonian fluid dynamics, heat/mass diffusion and transfer, polymer solidification, and related nonlinear instability at the transition from one stage to the next stage. Historically, Taylor [18] was the

pioneer in the study of electrospinning who first established a rigid self-similar theory for the Taylor cone with the half conic angle of 49.3°. The Taylor cone is the envelope cone of the sessile and pendent droplet of the liquid formed at the end of a capillary tube positioned in a steady electrostatic field of not very high amplitude. Spivak and Dzenis [19] provided an asymptotic solution for determining the shape of a weakly conductive droplet in electrostatic field. Yarin [20] advanced Taylor's work [18] by considering the non self-similar solutions to the hyperboloid-shaped liquid droplets, and found that the critical half conic angle of a droplet is 33.5°, which is much closer to the one observed in experiments. Besides, dynamic initiation of the Taylor cone from flat conductive liquids has also been studied within the framework of computational electrohydrodynamics and self-similarity theories [86, 87], among which the half-conic angle of the transient Taylor cone predicted by Reznik et al. [87] is $\leq 30°$, close to their experimental observations. These studies have clarified the physics of droplets before jet initiation in an electrostatic field. Once the jet initiates in the electrostatic field, it first forms a steadily accelerating straight jet as shown in figure 7 till it loses stability to form the whipping jet.

In this stage, several 1D electrohydrodynamic slender jet models have been formulated with different degree of elaboration. To study the asymptotic behavior of a straight jet accelerating in a steady electric field, Kirchenko et al. [88] formulated a 1D conductive jet model in which the liquid was treated as a simple newtonian fluid; this model predicts that the asymptotic jet radius has a power-law decay in the order of $z^{-1/4}$ with the distance z from the spinneret. By extending this model to weakly conductive non-newtonian fluids obeying the Oswald-deWaele power-law, Spivak and Dzenis [89] and Spivak, et al. [90] obtained the power-law asymptotic behavior of the jet radius, in which the index of the power-law decaying function is related to the flow index of the liquids. Hohman et al. [91, 92] formulated an elegant 1D slender jet model of newtonian fluids, in which the additional electric field due to the charged jet is also taken into account; this model is capable of providing the explicit characteristic relations of the jet axisymmetric and whipping instabilities [91-93] and examining the diameter dependency of electrospun nanofibers upon the material and process parameters, validated by experiments [94].

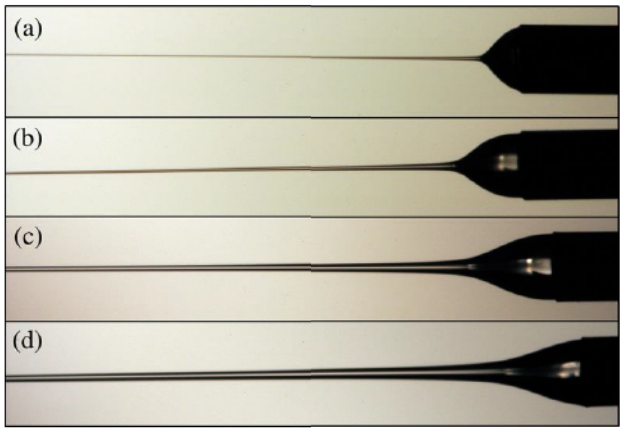

Figure 7. Steadily accelerating straight jets of 2% solutions of polyethylene oxide (PEO) (MW=920 kg/mol) in water. Initial jet diameter D=45 cm in all cases: (a) Flow rate Q = 0.02 ml/min and electric field E = 0.282 kV/cm; (b) Q = 0.10 ml/min and E = 0.344 kV/cm; (c) Q = 0.50 ml/min and E = 0.533 kV/cm; (d) Q = 1.00 ml/min and E = 0.716 [7]. Copyright (2007) of Elsevier.

In addition, Feng [95, 96] refined the 1D jet model by Hohman et al. [91, 92] to eliminate several existing incompatibilities of the boundary conditions at the nozzle tip, and to further tackle the effect of non-newtonian and viscoelastic fluid models on the jetting behavior of an charged jet in an electrostatic field. Yet, to model a realistic electrospinning process, even at the very beginning stages, the liquids of the above models should be matched to the flow in the droplet region at the outlet of the nozzle. In this region, the flow becomes fully two-dimensional (2D axisymmetric) and the slender jet models can be only considered as the first-order approximation [3]. Though a few fully 2D numerical simulations have been devoted to understanding the transition zone between the droplet and the electrically driven jet [97-99], no complete, robust jet model has been available yet to capture the entire electrohydrodynamic phenomenon from the jet initiation to whipping destabilization in a conventional nozzle-based electrospinning process.

Nevertheless, to elucidate the jet bending (whipping) instability in electrospinning, Reneker et al. [100, 101] developed a reduced bead model in which the jet is simply modeled as a chain of charged beads linked through linearly elastic springs and viscous dashpots in series based on a viscoelastic Maxwellian model. This model can reasonably explain the phenomenological jet bending instability, jet conical envelope, drying process, interaction of multiple jets, and study of the effect of process parameters of electrospinning, among others [60, 102-104]. More recently, Dayal and Kyu [105] and Dayal et al. [106] developed a 3D spring-network model coupled with phase separation and solvent evaporation to capture the spatio-temporal evolution of phase separation in a polymer-solution jet during electrospinning. This model can be used to quantitatively explain a few coupled multi-physics phenomena involved in polymer nanofiber formation in electrospinning.

In addition, the above jet models were built on a homogeneous jet. However, the solvent evaporation from the jet surface during electrospinning may lead to inhomogeneity in an instantaneous jet in both the radial and axial directions of dilute polymer jets. Solvent evaporation even becomes very fast in an ultrathin jet. Thus, solvent evaporation plays a crucial role in nanofiber formation by means of electrospinning. Recently, Wu et al. [107] developed a simple 1D axisymmetric jet model to simulate the drying process of an electrospun jet of dilute polymer solution, in which the jet was simplified an ultrathin cylinder of polymer solution.

Phenomenologically, the drying process of a jet suspended in air involves three successive sub-processes [107]: (1) diffusion of solvent molecules from the inside of the jet to its surface, (2) evaporation of solvent molecules from the jet surface, and (3) transport of solvent vapor from the jet surface into the bulk of the atmosphere. In electrospinning, a significant jet shrinking happens due to evaporation of a significant volume of solvent from the dilute solution jet. This model is based on three fundamental assumptions that have been generally used in simulation of drying process of coating systems [107-109]: (1) due to the small jet diameter, the temperature field is considered constant inside the jet; (2) the drying process involving solvent diffusion and transfer is treated as axisymmetric; (3) the effect of residual stresses due to solvent loss on the jet solvent diffusion and transfer is negligible; (4) micro convection due to vapor concentration gradient near the jet is negligible; (5) no chemical reactions take place inside the jet. These assumptions can approximately hold for an ultrathin jet. Thus, for a binary polymer solution used in electrospinning, the governing equation of mass diffusion in an electrospun axisymmetric jet was derived according to the axisymmetric Fick's law of mass diffusion [107]:

$$\frac{\partial C_1}{\partial t} = \frac{1}{r}\frac{\partial}{\partial r}(Dr\frac{\partial C_1}{\partial r}), \tag{1}$$

the initial conditions at the beginning of the drying process are assumed as

$$t = 0: \qquad C_1 = C_{10}, \ R_0(0) = R_0, \tag{2}$$

and the boundary conditions at the center and moving surface of the jet are

$$r = 0: \qquad \partial C_1 / \partial r = 0, \tag{3}$$

$$r = R_0(t): \qquad \frac{D}{1-\bar{V}_1 C_1}\frac{\partial C_1}{\partial r} = -\frac{k_g M_1 (P_s - P_\infty)}{RT}, \tag{4}$$

$$r = R_0(t): \qquad \frac{dR_0(t)}{dt} = -\frac{k_g M_1 \bar{V}_1}{RT}(P_s - P_\infty). \tag{5}$$

In the above, C_1 is the transient solvent mass concentration in the polymer solution with its initial value C_{10} as constant over the jet cross-section; R_0 is the initial jet radius; $R(t)$ is the current jet radius; k_g (cm/g) is the coefficient of solvent mass transfer at the jet surface; M_1 is the solvent molar weight; $\bar{V}_1$ is the solvent specific partial volume; T is the absolute temperature near the jet surface; R = 8.3144 J/mol is the universal gas constant; P_∞ is the solvent vapor pressure in the atmosphere far from the jet surface (P_∞ = 0 used in the current simulation [107]); P_s is the solvent saturation vapor pressure near the jet surface.

The dependence of P_s upon the solvent concentration near the jet surface can be approached according to the Flory-Huggins equation [110]: $P_s/P_0 = \varphi_1 \exp(\varphi_2 + \chi\varphi_2^2)$, where P_0 is the saturation vapor pressure of the pure solvent, ϕ_1 and ϕ_2 ($\phi_2 = 1-\phi_1$) are the solvent and polymer volume fractions, respectively, and χ is the Flory-Huggins polymer/solvent interaction parameter. χ can be approximated by using Bristow's semi-empirical equation [111, 112]: $\chi = 0.35 + (\delta_1 - \delta_2)^2 \tilde{V}/(RT)$, where $\tilde{V}$ is the solvent molar volume, and δ_1 and δ_2 are the solubility parameters of the solvent and polymer, respectively. In the simulation [107], the value of χ is selected as a constant (i.e., χ = 0.45). The polymer/solvent mutual diffusion coefficient D is described by the Vrentas-Duda free-volume theory [113, 114]: $D = D_1(1-\varphi_1)^2(1-2\chi\varphi_1)$, where D_1 is the solvent self-diffusion coefficient. The above governing partial differential equation (PDE) (1) under the initial and boundary conditions (2-5) can be solved efficiently by using an explicit backward-finite difference method (FDM) [115] based on a moving grid scheme [107].

Wu et al. [107] considered the drying process of a PAN/DMF jet with the initial DMF mass concentration 88%. It needs to be mentioned that the PAN/DMF solution is technologically important as it is commonly used to produce precursors for long carbon nanofibers (CNFs) [116, 117]. In the simulation, the material parameters of the PAN/DMF

solution are the follows. The mass densities of DMF (M_w = 73) and PAN (M_w = 150,000) are ρ_{DMF} = 0.944 g/cm^3 and ρ_{PAN} = 1.184 g/cm^3, respectively. The PAN diffusion coefficient in infinite DMF is D_1 = ~1.5×10^{-6} cm. The DMF saturation vapor pressure at 20°C is ~500 Pa. The DMF mass transfer coefficient at the jet surface is k_g = ~0.2 m/s, by analogy with similar solvents [118]. The initial DMF mass ratio of 88% corresponds to C_1 = 0.851. Figures 8 and 9 show the typical numerical results of the drying process of a PAN/DMF jet with varying initial diameter [107]. The numerical results in figure 8 show that solvent evaporation results in inhomogeneity of the solvent concentration in microscopic jets, and such inhomogeneity mitigates with decreasing initial jet radius. Significant jet shrinking due to solvent loss can be also clearly observed.

The numerical results indicate that the composition of the jet could be highly inhomogeneous across the jet due to fast solvent evaporation especially near the jet surface; such inhomogeneity may further influence the rheological properties of an electrospun jet and thus affect the electrohydrodynamic process of the whipping jet, drying duration (figure 9), and resulting nanofiber properties such as the final fiber diameter, fiber morphology [119,120], and mechanical properties, among others.

It needs to be noted that the above 1D drying jet model has oversimplified the electrohydrodynamic effect on the solution diffusion and transfer. During the process, themodel has separated the jet electrohydrodynamics from its mass diffusion and transfer. In reality, such two phenomena are coupled to determine the evolution of the jet diameter.

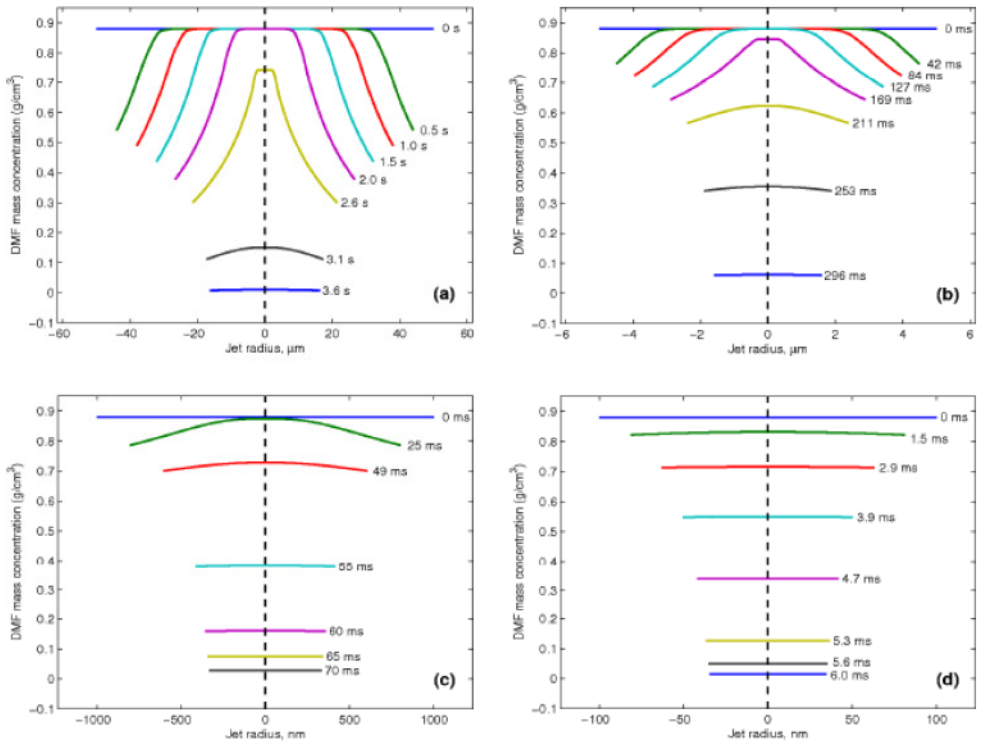

Figure 8. Numerical results of instantaneous solvent (DMF) mass concentration profiles in PAN/DMF solution jets with the initial radii: (*a*) R_0 = 50 μm, (*b*) 5 μm, (*c*) 1000 nm, and (*d*) 100 nm, respectively [107]. Copyright (2011) of the American Institute of Physics.

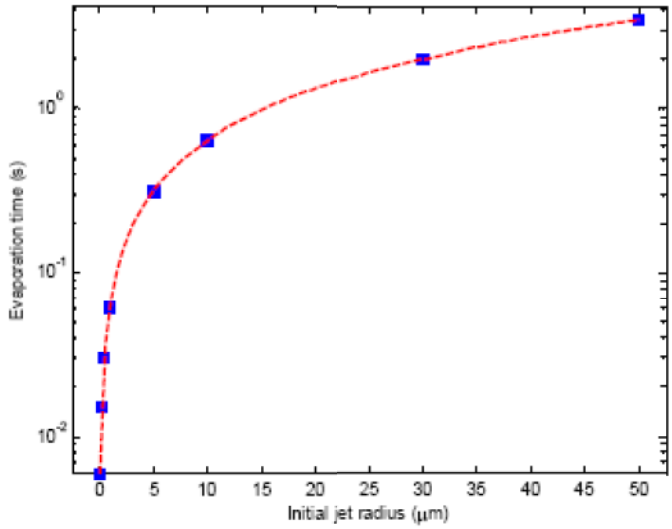

Figure 9. Numerical results of variation of the drying duration with the initial jet radius [107]. Copyright (2011) of the American Institute of Physics.

Therefore, new theoretical effort is still desired in order to gain in-depth understanding of the entire electrospinning process, particularly the various destabilizations, drying process and drying induced nanostructured surface morphology and porous structure formation. These models are expected useful to guide the conventional nozzle-based electrospinning experiments and development of new, innovative models to capture the entire process of needleless electrospinning for production of mass nanofibers [107].

MECHANICAL CHARACTERIZATION OF ELECTROSPUN NANOFIBERS

Similar to other nanostructured and bulk materials, mechanical properties of electrospun nanofibers (e.g., modulus, tensile strength, yielding behavior, etc.) are fundamental to fulfill their targeted structural and functional applications. In the view of end use of nanofibers, controlled electrospinning process is desirable for production of continuous nanofibers carrying with tailorable geometries, stiffness and strength. In addition, the high surface area to volume ratio of nanofibers and their unique manufacturing method may result in the mechanical properties essentially different from those of their bulk counterparts.

Such unique mechanical propertiesmay further influence the deformation, dynamics, stability, adhesion/contact/friction, wetting, and global mechanical response of the resulting nanofibers and nanofiber networks [121-150]. In recent years, cutting-edge micro and nanomechanical characterization techniques [132, 135-150] have been explored for understanding the mechanical response of individual nanofibers produced by electrospinning. Among these, atomic force microscope (AFM) has been widely used for axial modulus and tensile strength measurements of electrospun nanofibers in several groups [136, 138, 139, 141-143]. To date, four AFM-based testing methods have been formulated including AFM-based axial tension test [135, 141], three-point bending test [136, 138, 142], double-beam vibration test [143], and nanoindentation. In an AFM-based axial tension test, the nanofiber

segment is fixed between the AFM tip and the substrate (e.g., silicon wafer) by using adhesive.

The tiny tensile force is exerted via the motion of the AFM tip. In contrast, for a micro three-point bending test of nanofibers as shown in figure 10, the nanofiber segment is first clamped across a groove on the substrate using adhesive [136, 138, 142]. The lateral force to induce the deflection is exerted through the AFM tip at the midspan of the fiber segment. In principle, the axial modulus of nanofibers can be also measured by means of nanoindentation similar to that for characterization of thin films. After each test, a force-deformation diagram is obtained, from which the modulus can be extracted. The axial modulus can be also extracted from the resonant frequencies of a pair of microcantilevers linked by the nanofiber segments [143].

In addition, the axial modulus and tensile strength of nanofibers can be also estimated from the average axial modulus and tensile strength of a bundle of nanofibers that can be measured using a microtensile device [142]. Yet, AFM-based testing methods have the technical barriers in determining the ultimate tensile strength and strain to failure of nanofibers. Moreover, idealized experimental conditions such as the clamped ends introduced in three-point bending tests for data reduction may further induce additional deviation of the measurements.

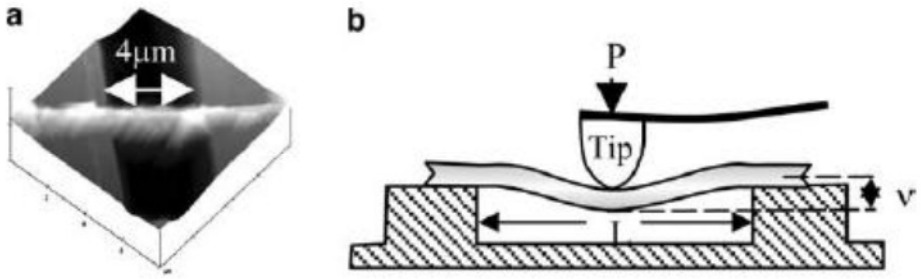

Figure 10. (*a*) AFM contact mode image of a single nanofiber of diameter ~400 nm suspended over an etched groove; (*b*) schematic setup of an AFM-based three-point bending test of electrospun nanofiber [136]. Copyright (2004) of the American Institute of Physics.

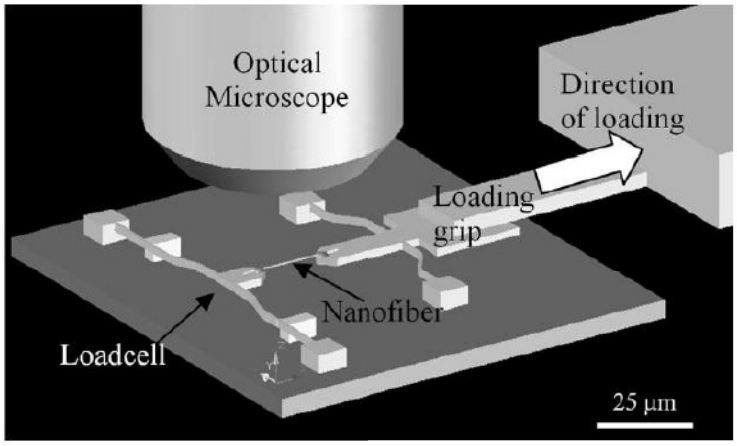

Figure 11. A microtensile testing platform for mechanical characterization of electrospun nanofibers [144,145]. Copyright (2007) of the American Institute of Physics.

Yet, the preferable method for mechanical characterization of nanofibers would be directly testing the individual nanofibers based on micro/nano tensile testers installed with a high-resolution load cell and position controller. Recently commercialized universal micro/nano tensile testers such as the Nano Bionix® and Nano UTM® by Agilent® and microelectromechanical systems (MEMS)-based micro tensile testers (figure 11) have reached the capability of accurately measuring the load-displacement relationship of single nanofibers and nanowires [144-146].

As a result, the full-range stress-strain diagram of a single nanofiber can be determined accurately. For instance, by using a Nano Bionix® machine, Tan et al. [137] have successfully performed the uniaxial tension test of electrospun polycaprolactone (PCL) fibers with the fiber diameters of ~1 μm as shown in figure 12, and they pointed out that the stress-strain diagram of the PCL nanofibers exhibited obvious size effect, i.e., both the ultimate tensile strength and yield stress decrease with increasing fiber diameter while the failure strain increases with the increase of fiber diameter. No noticeable correlation was established between the axial modulus and fiber diameter [137].

Similarly, Chen et al. [132] used a lab-made high-resolution micro tensile station, similar to the Nano UTM® to characterize the modulus and tensile strength of electrospun polyimide [poly(*p*-phenylene biphenyltetra-carboximide), BPDA/PPA] (PI) nanofibers with the diameter of ~300 nm. The experimental results showed that the PI nanofibres had an average ultimate tensile strength of 1.7 ± 0.12 GPa, axial tensile modulus of 76 ± 12 GPa, and ultimate strain of ~3%. These experimental measurements were among the highest ones reported in the literature to date.

In contrast, the precursor nanofibres with the similar fiber diameters and molecular weights carried the average ultimate tensilestrength of 766 ± 41MPa, axial modulus of 13 ± 0.4GPa and ultimate strain of ~43%. In these tension tests, the reliability of the experimental results depends upon the accurate measurement of tensile force, which is in the range from a few millinewtons (μNs) to micronewtons (mNs).

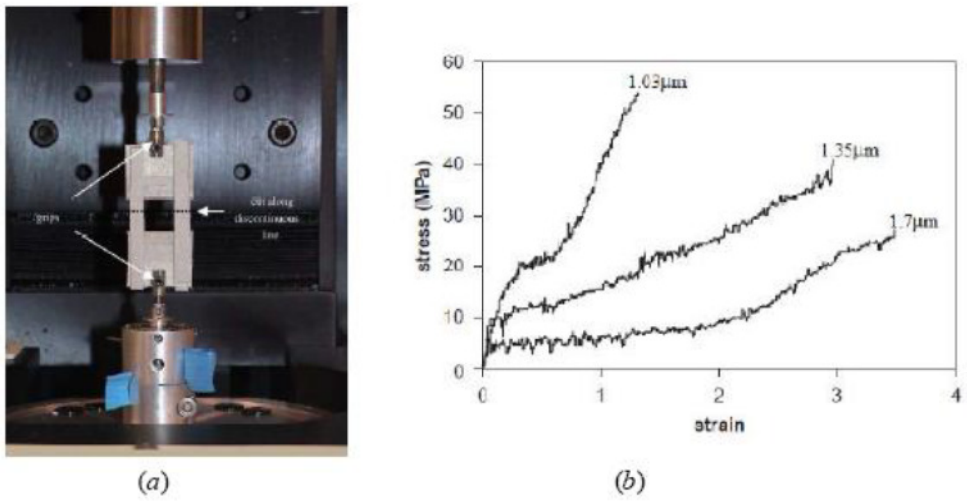

(*a*) (*b*)

Figure 12. (*a*) Microtensile testing setup based on Nano Bionix® in which a single nanofiber is mounted on a cardboard sample-template; (*b*) stress-strain diagrams of three electrospun polycaprolactone (PCL) nanofibers of varying diameters [137]. Copyright (2005) of Elsevier.

In an attempt to accurately capture the tiny tensile forces in a single-nanofiber tension test, recently developed MEMS-based microtensile testers offer an excellent alternative in the view offeasibility and accuracy of the mechanical characterization [144-146], in which the tensile force can be precisely recorded and the loading rate can be controlled extremely lower compared to other micro tensile testers such as Nano Bionix® and Nano UTM®.

To date, increasing experimental results have been accumulated on the mechanical properties of electrospun nanofibers that have greatly enriched the database for in-depth study of the mechanical response of electrospun nanofibers and their dependencies upon the geometric, material, and process parameters. Among others, two unique mechanical behaviors of electrospun polymer nanofibers have been identified experimentally that are essentially different from their large-diameter and bulk counterparts. The first unique discovery is that the axial modulus and ultimate tensile strength of electrospun polymer nanofibers increase abruptly when the fiber diameter is below a certain value [126, 135, 141, 142, 147]. One example is shown in figure 12(b), where the ultimate tensile strength of electrospun PCL nanofibers is nearly doubled when the fiber diameter is decreased from 1.7 μm to 1.03 μm. Ji et al. [151] also discovered that polystyrene (PS) nanofibers quickly increased the axial modulus when their diameters were below ~500 nm; in the case of electrospun poly(2-acrylamido-2-methyl-1-propanesulfonic acid) (PAMPS) nanofibers, they found that such phenomenon was obvious such that the axial modulus increased from ~300 MPa at the diameter of ~110 nm up to ~2.0 GPa when the diameter is ~55 nm. It needs to be mentioned that though the size effect in the mechanical properties of nanomaterials has been widely accepted, it happens at the threshold dimension (i.e., fiber diameter) is much larger than that in metallic nanostructures. Several potential factors may contribute to such size effect, including surface energy [123, 126], chain alignment, and formation of crystalline and semicrystalline structures [140] (figure 13), among others. However, the pure contribution of surface energy is insufficient to interpret such an abrupt increase in the modulus and tensile strength of polymer nanofibers. Besides, the alignment of polymer chains can be also induced in the electrospinning process, in which the electrostatic stretching and constrained polymer chain motion inside the ultrathin jet can contribute the alignment. Nevertheless, recent X-ray diffraction results of electrospun Nylon (polyamide, PA) nanofibers indicated that only a mild monotonous increase can be identified in the crystallinity and orientation of the crystallites inside the electrospun polymer nanofibers with varying fiber diameters [147]. Thus, such a mild increase is also not sufficient to account for the observed large increase in the axial modulus. In addition, the study also pointed out that the average size of crystallites (~4 nm) was largely independent of the fiber diameter. As a result, the crystallinity inside the electrospun PA nanofiberswas nearly constant in the range of fiber diameter under the experimental investigation. To explore the potential physical mechanism of the observed obvious size effect in the tensile modulus of electrospun polymer nanofibers, recently Arinstein et al. [147] proposed the concept of supramolecular structure of amorphous phase in electrospun polymer nanofibers. Such supramolecular structure is made of oriented fragments of polymer chains that may form when the polymer chains are confined inside the polymer nanofibers with the fiber diameter below a certain value. Based on this conceptual model, a preliminary estimate of the transition fiber diameter, below which the polymer nanofibers may exhibit observable size effect in their mechanical properties, is close to those observed in experiments [147]. Yet, this conceptual approach still leaves an outstanding issue: what

mechanism governs the likely power-law growth of the axial modulus of electrospun polymer nanofibers with the decrease of fiber diameter below a certain value [126].

Furthermore, surface rippling is another unique phenomenon that was discovered recently in compliant polymer nanofibers (e.g., as-electrospun PAN nanofibers) subjected to axial stretching. Surface rippling or wrinkling can be commonly triggered in compressed compliant surface. Such surface instability in polymer nanofibers was first discovered in MEMS-based micro tension tests of as-electrospun PAN nanofibers [144, 145, 150]. During the tests, periodic ripples suddenly appeared on the fiber surfaces once the axial stretch reach a certain threshold as shown in figure 13 [144, 145, 150]. During the process, the nanofibers did not exhibit obvious softening, and the axial strain to failure (in sense of engineering strain) measured in single-fiber tension tests was up to 60%-130% for as-electrospun PAN nanofibers with the diameter in the range of~300-600 nm. This axial strain is several folds of that measured from PAN microfibers produced via drawing or dry-jet-wet spinning [144, 145]. Such a large axial strain to failure can be attributed to the simultaneous surface rippling of the nanofibers and relevant global softening, which induces the plastic strain much larger than that due to single necking failure in classic polymer microfibers. To explore the physical mechanism of the surface rippling in as-electrospun polymer nanofibers, Naraghi et al. [144, 145] proposed that there exist periodic distribution sites to accommodate the local instabilities. Furthermore, they pointed out that fine circumferential surface cracks were detected on the surface of nanofibers under stretching, and these surface cracks could facilitate the seeking of necking, analogous to fragmentation as evidenced in hard-film-on-soft-substrate systems. Yet, no qualitative and quantitative correlationswere made between the nearly constant wavelength of the periodic surface ripples and the geometrical and material parameters of the nanofibers. In reality, surface defects, voids, and cracks commonly exist on fiber surface, however, subjected to axial stretching, some surface cracking is suppressed while some other ones were enhanced due to the specific instability conditions as treated theoretically by Wu et al. [126] and Wu [127] (See the next section).

Such surface rippling was also observed in pulled-out PAN nanofibers during interlaminar fracture test of polymer composites, in which the electrospun PAN nanofibers were entangled at ply interfaces as nanoreinforcement, as shown in figure 14. In addition, surface ripples were also observed in electrospun polyimide (PI) nanofibers after annealing as shown in figure 15. Figure 15(*a*) shows the image of an as-electrospun PI nanofiber characterized by means of AFM; it can be observed that the as-electrospun PI nanofiber was very smooth. However, when the smooth PI nanofibers were deposited on a silicon wafer in electrospinning andannealed (a process of imidization) at ~400°C in nitrogen environment, surface ripples occurred. Such rippling phenomenon may be related to the axial shrinking during the imdization process.

In principle, formation of surface ripples on the surface of electrospun nanofibers is a phenomenon of surface destabilization that could be correlated to the combined effect of surface tension and nonlinear elasticity of the compliant polymer nanofibers. To date, necking and surface destabilization of classic elastic bars of large diameter subjected to finite axial stretch has been well studied within the framework of nonlinear elasticity in classic solid mechanics [152-154]. In such a study, the effect of surface energy of the elastic bars was very small and therefore ignored due to the large characteristic dimension (diameter) and high elastic modulus of the elastic rods. In contrast, when the fiber diameter is reduced down to nanoscale, the surface tension (surface energy) of the compliant nanofibers may dominate the

initiation and propagation of surface rippling. Thus, new theoretical justification is desirable for such a unique surface destabilization phenomenon. Beyond this, due to the unique small characteristic dimensions and very low stiffness of the electrospun polymer nanofibers, systematic theoretical studies are desired to count for the deformation, contact, adhesion, and other mechanical behavior of these ultrathin compliant nanofibers where the effect of surface energy would be taken into account.

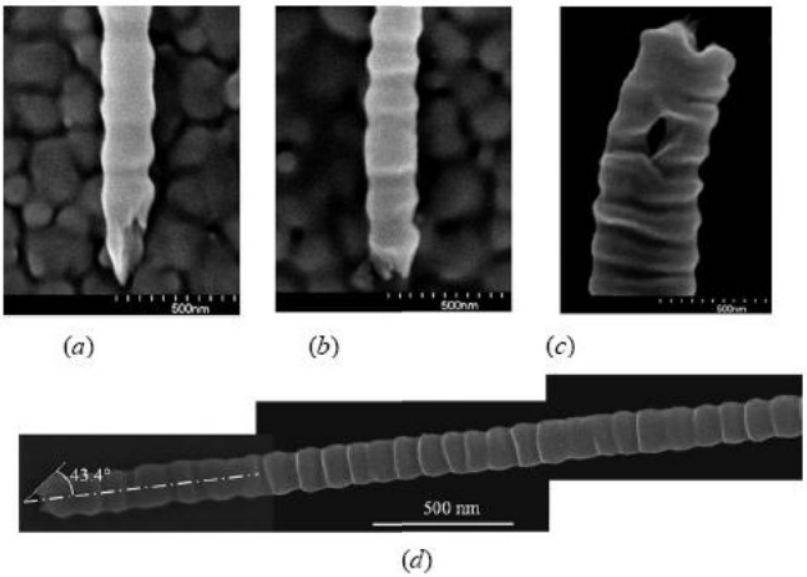

Figure 13. [(*a*) and (b)] SEM micrographs of surface morphology of as-electrospun PAN nanofibers after tensile breakage; the fiber breakage was induced by extrusion of a 45° conic region; (*c*) SEM micrograph of a fiber breakage due to the formation of voids; (*d*). SEM micrograph of ripples formed on the PAN nanofiber surfaces subjected to axial stretching [144]. Copyright (2007) of the American Institute of Physics.

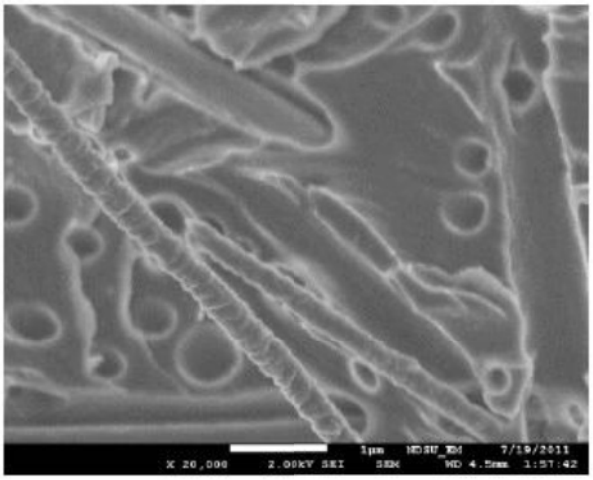

Figure 14. SEM micrograph of the surface morphology of electrospun PAN nanofibers with surface rippling. The PAN nanofibers were inserted at the interfaces of carbon-fiber fabric/epoxy composites and pulled out after mode I interlaminar fracture test.

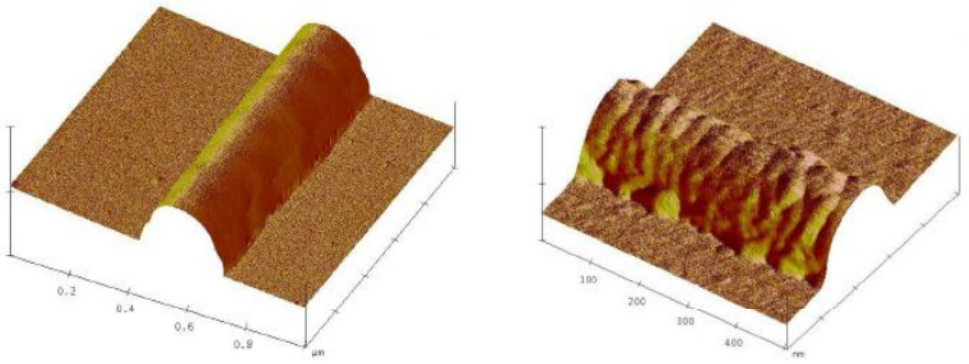

(*a*) (*b*)

Figure 15. 2 AFM micrographs of surface morphology of (*a*) as-electrospun PI precursor nanofiber and (*b*) PI nanofiber after imdization (fiber diameter: ~250 nm) [126]. Copyright (2008) of the American Physical Society.

MODELING OF MECHANICAL BEHAVIOR OF ELECTROSPUN NANOFIBERS

Phenomenological mechanics models are useful to rationally understand the mechanical behavior of electrospun nanofibers subjected to various loading and environmental effects such as axial tension, contact and adhesion, wave propagation, surface ripping, and wetting, among others. In the recent years, the first author and his co-workers have proposed several continuum mechanics models [121-131] to quantitatively approach the mechanical response of nanofibers by taking into account the effect of surface energy. Due to introduction of the new material parameter of surface energy (surface tension γ: J/m^2) to the nanofiber models, a new intrinsic dimensional parameter $l_0=\gamma/E$ (E: elastic modulus) appears naturally during the modeling process, which can be treated as a criterion whether or not to consider the size effect of the polymer nanofibers. Basically, when the characteristic dimension (i.e., fiber diameter d) is comparable to l_0, the size effect due to the surface energy is appreciable; otherwise, the size effect can be safely ignored, i.e., the surface energy can be ignored in the modeling. It needs to be noted that for polymer nanofibers, especially for those of ultra compliant polymer nanofibers, their moduli are orders lower than those of metallic materials. Therefore, the intrinsic dimensional parameter l_0 of compliant polymer nanofibers is orders larger than those of metallic materials. As a result, compliant polymer nanofibers behave more obvious size effect compared to metallic nanomaterials. In the below, we briefly review several mechanics models relating the mechanical behavior of single nanofibers and fiber networks.

1. Contact and Adhesion of Nanofibers [124]

In electrospinning process, the polymer nanofibers are collected in the form of nonwoven nanofiber mat, in which contact and adhesion between nanofibers is the most common phenomenon.

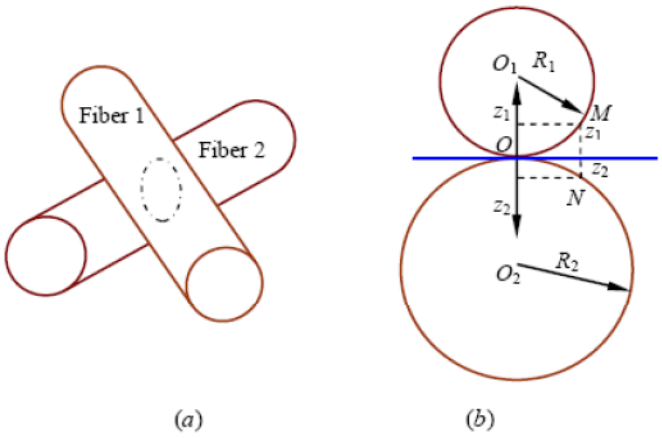

Figure 16. Cylindrical filaments in contact (*a*) contact zone between filaments in contact (*b*) coordinate systems [124]. Copyright (2007) of the Institute of Physics.

The simplest model to count for adhesive contact between nanofibers can be established using the principle of elastic contact between two elastic cylinders positioned in an arbitrary angle and with consideration of the effect of surface adhesion [124]. Such a contact problem can be treated as a special case of the DMT (Derjaguin-Muller-Toporov) theory [155] or the generalized Hertz contact theory [156-159].

Here, let us first consider the classic Hertz contact theory for the contact of two elastic bodies positioned in an arbitrary angle as shown in figure 16. Establish the (x,y)-plane tangent to both the cylindrical surfaces of the cylinder contacting at the origin O. The curvilinear surfaces near the contact point O can be described using two polynomials (ignore the high-order terms):

$$z_1 = A_1x^2 + A_2xy + A_3y^2.$$
$$z_2 = B_1x^2 + B_2xy + B_3y^2. \tag{6}$$

The distance (gap) between two points at the two curvilinear surfaces such as M and N [see figure 16(*b*)] is

$$z_1 + z_2 = (A_1 + B_1)x^2 + (A_2 + B_2)xy + (A_3 + B_3)y^2, \tag{7}$$

where A_i (i = 1, 2, and 3) and B_i (i = 1, 2, and 3) are the geometrical parameters that are determined by the surfaces near the contact point above and below. By properly selecting the (x, y)-coordinate system, the cross term xy can be eliminated. Thus, relation (7) can be simplified as

$$z_1 + z_2 = Ax^2 + By^2, \tag{8}$$

where A and B are coefficients relevant to the principal curvatures of the surfaces in contact and the orientation angle between the two cylinders as

$$A+B=\frac{1}{2}(\frac{1}{R_1}+\frac{1}{R_1'}+\frac{1}{R_2}+\frac{1}{R_2'}),$$
$$B-A=\frac{1}{2}[(\frac{1}{R_1}-\frac{1}{R_1'})^2+(\frac{1}{R_2}-\frac{1}{R_2'})^2+2(\frac{1}{R_1}-\frac{1}{R_1'})(\frac{1}{R_2}-\frac{1}{R_2'})\cos 2\varphi]^{1/2}. \quad (9)$$

In the above, R_1 and R_1' are the principal radii of curvature of the curvilinear surface above; R_2 and R_2' are those of the curvilinear surface below; φ is the orientation angle between the two axes of the cylinders. In the case of two fibers with the equivalent diameter R and fiber orientation angle φ, the coefficients A and $B$are

$$A=\frac{1-\cos\varphi}{2R},\ \ B=\frac{1+\cos\varphi}{2R}. \quad (10)$$

Theory of elasticity [157] shows that the sum of the displacements w_1 and w_2 of the points on the curvilinear surfaces in contact above and below is

$$w_1+w_2=(k_1+k_2)\int\frac{p}{r}dA, \quad (11)$$

where pdA is the pressure exerted on an elemental area of the contact surface, r is the distance from this elemental area to the contact center [see figure 16(b)], and k_1 and k_2 are two parameters defined by

$$k_1=\frac{1-\nu_1^2}{\pi E_1},\ k_2=\frac{1-\nu_2^2}{\pi E_2}, \quad (12)$$

where E_i and ν_i (i=1,2) are Young's moduli and Poisson's ratios of the elastic bodies above and below, respectively. The integration (11) must be considered over the entire surface in contact:

$$(k_1+k_2)\int\frac{p}{r}dA=\alpha-Ax^2-By^2, \quad (13)$$

where α the distance reduction between the two elastic bodies subjected to compression, and w_1 and w_2 the displacements of the points on the surfaces in contact above and below, respectively.

Hertz contact theory [156-158] gives the pressure p over the contact surface to satisfy Eq. (13) that is represented by the ordinates of a semi-ellipsoid spanning on the entire contact surface. The peak pressure p_0 is located at the center of the contact zone. By denoting a and b as the semi-axes of the ellipse of the contact zone, the peak pressure can be determined by

$$P=\int pdA=\frac{2}{3}\pi abp_0, \quad (14)$$

and

$$p_0 = \frac{3}{2}\frac{P}{\pi a b}. \tag{15}$$

In the above, P is the compressive force. In the case of polymer nanofibers, P is the resultant adhesive force between two nanofibers in contact that can be estimated by some adhesive theory. The peak pressure is 1.5 times the average pressure on the contact surface, and α is related to the compressive force P and the semi-axes of the ellipse a and b [157]:

$$\alpha = \frac{3P(k_1+k_2)}{4}\int_0^\infty \frac{d\xi}{\sqrt{(a^2+\xi)(b^2+\xi)\xi}}, \tag{16}$$

where the semi-axes a and b are determined as

$$a = m\sqrt[3]{\frac{3\pi}{4}\frac{P(k_1+k_2)}{A+B}}, \quad b = n\sqrt[3]{\frac{3\pi}{4}\frac{P(k_1+k_2)}{A+B}}. \tag{17}$$

In above coefficients m and n are numbers depending only on the ratio $(B\text{-}A)$ to $(A+B)$ as tabulated in Table 1 [157].

The compressive force between two contacting nanofibers can be understood as adhesive forces which can be approximated according to Bradley's approach [160]. In this approach, the adhesive force between two unit areas is assumed to follow the long-range Lennard-Jones force:

$$\sigma(z) = \frac{8\Delta\gamma}{3\varepsilon}[(\frac{\varepsilon}{z})^3 - (\frac{\varepsilon}{z})^9]. \tag{18}$$

In the above, ε is a phenomenological distance between two atoms/molecules; z is the distance between two unit areas; and $\Delta\gamma$ is Dupré adhesion energy that is defined by

$$\Delta\gamma = \gamma_1 + \gamma_2 - \gamma_{12}, \tag{19}$$

where γ_1 and γ_2 are respectively the surface energies of the filaments, and γ_{12} is the interface energy. For two equivalentnanofibers in contact, $\Delta\gamma=2\gamma$. Thus, the adhesive force between two contacting nanofibers can be determined by performing the following integration

$$P = \frac{8\Delta\gamma}{3\varepsilon}\int_A \sigma(z)dA = \frac{8\Delta\gamma}{3\varepsilon}\int_A [(\frac{\varepsilon}{Ax^2+By^2-\alpha+h_0})^3 - (\frac{\varepsilon}{Ax^2+By^2-\alpha+h_0})^9]dA, \tag{20}$$

where the integration domain is over the region out of the contact zone on the tangential plane, i.e., $Ax^2+By^2 \geq \alpha$, h_0 is the minimum gap between surfaces in contact.

Table 1. *m* and *n* values for varying angle φ [157]

θ^o	30^o	35^o	40^o	45^o	50^o	55^o	60^o	65^o	70^o	75^o	80^o	85^o	90^o
m	2.731	2.397	2.136	1.926	1.754	1.611	1.486	1.378	1.284	1.202	1.128	1.061	1.000
n	0.493	0.530	0.567	0.604	0.641	0.678	0.717	0.759	0.802	0.846	0.893	0.944	1.000

According to Bradley's approach, it assumes $h_0 = \varepsilon$. Substitution of (10) into (20) leads to the compressive force P [124]:

$$P = \frac{4\pi\gamma R}{\sin\varphi}. \tag{21}$$

Consequently, the semi-axes of the elliptical contact zone can be determined by substituting (10) and (21) into (17) as

$$a = m\sqrt[3]{\frac{6\pi(1-\nu^2)}{\sin\varphi}\frac{R^2\gamma}{E}},\quad b = n\sqrt[3]{\frac{6\pi(1-\nu^2)}{\sin\varphi}\frac{R^2\gamma}{E}}, \tag{22}$$

and m and n are two functions with respect to φ, respectively, as tabulated in Table 1 [157]. The distance reduction of the nanofibers α due to the distributed adhesive forces over the two curvilinear surfaces can be determined by substituting (21) and (22) into (13):

$$\alpha = \frac{6\pi(1-\nu^2)}{\sin\varphi}\frac{\gamma R}{E}\int_0^\infty \frac{d\xi}{\sqrt{(a^2+\xi)(b^2+\xi)\xi}}. \tag{23}$$

The above relations (20-23) govern the adhesive contact in polymer nanofibers. As an example, the area of the contact zone can be determined by relation (22) as

$$A_c = \pi ab = \pi mn\left[\frac{6\pi(1-\nu^2)}{\sin\varphi}\frac{R^2\gamma}{E}\right]^{2/3}. \tag{24}$$

When the two fibers are cross-positioned (orthogonal), the area of the contact zone reaches its minimum value as [124]

$$(A_c)_{\min} = 6^{2/3}\pi^{5/3}(1-\nu^2)^{2/3}(\frac{R^2\gamma}{E})^{2/3}. \tag{25}$$

Figure 17 shows the numerical results of the area of contact zone with varying fiber diameters and fiber surface tension [124]. In the numerical process, the surface tensions of the nanofibers are selected as γ=0.05 N/m and γ = 0.1 N/m, respectively. The Young's modulus of the fibers is given as E=20 GPa. Two families of polymer nanofibers are used. The first family has the fiber radii of 2μm, 5μm, 10μm, 15μm, and 20μm; and the second has the fiber radii of 100nm, 200nm, 500nm, 1000nm, and 1500nm.

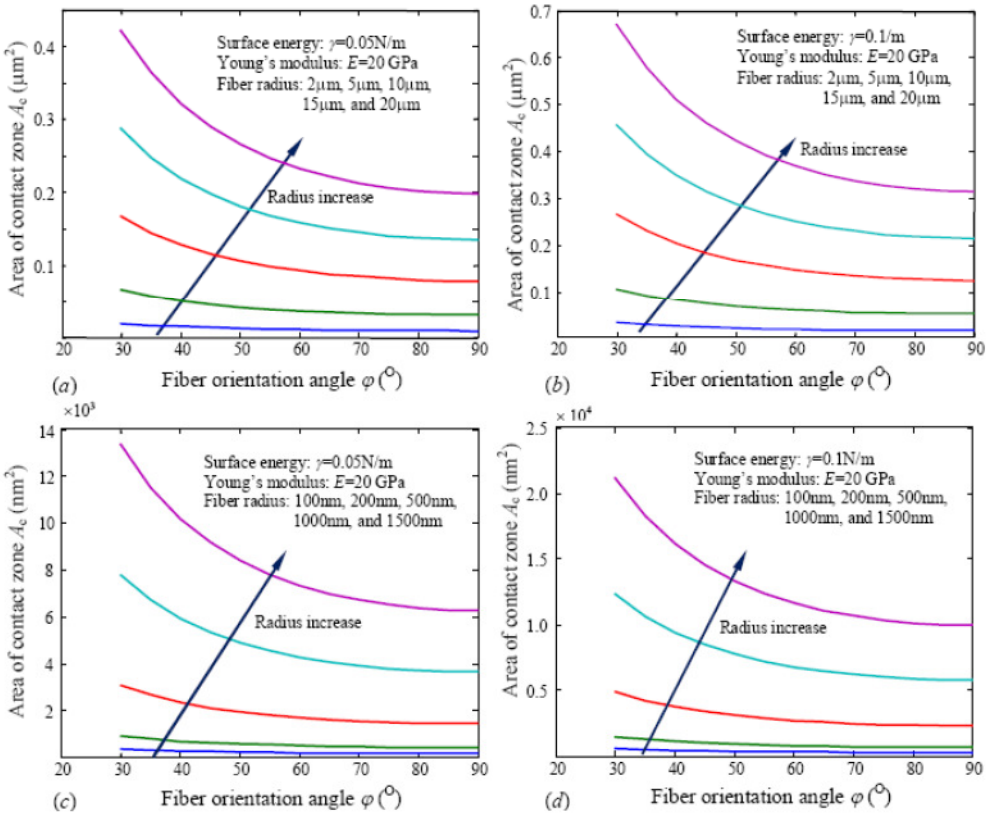

Figure 17. Variation of the area of contact zone vs. the angle between fibers (*a*) γ= 0.05N/m and (*b*) γ= 0.1N/m for fiber radii of 2μm, 5μm, 10μm, 15μm, and 20μm, respectively, and (*c*) γ= 0.05N/m and (*d*) γ= 0.1N/m for fiber radii of 100nm, 200nm, 500nm, 1μm, and 1.5μm, respectively [124]. Copyright (2007) of the Institute of Physics.

It can be observed from figure 17 that at a given polymer nanofiber radius, the contact are decreases rapidly with increasing angle φ between two fibers due to the rapid decrease of adhesive force with growing angle φ [124].

The above model can be used for determining the contact force, contact stress, and area of contact zone. The results given by the above model can be consideredfor exploring the mechanisms of nanofiber friction, sliding, and compression hysteresis in nanofibrous materials subjected to external loading. These parameters are expected important when taking into account the mechanical response of ultrathin soft nanofibers, where the adhesive force-induced contact will result in significant deformation and stresses in the nanofibers.

2. Collapse of Adhesive Nanofibers [125]

In electrospinning, the nanofibers are commonly collected as porous nonwoven nanofiber mat, where a majority of fibers are suspended. Besides, in many nanofiber-related applications such as nanofiber sensors and transducers, the nanofibers will work as free-standing member. Thus, adhesion between the nanofiber and surroundings (e.g., other nanofibers, substrates, etc.) may significantly influence the performance of the nanofiber.

Herein, we define the phenomenon that due to external perturb, a nanofiber is stuck to another nanofiber or substrate as nanofiber *collapse*. Figure 18 shows a typical example of nanofiber collapse due to surface adhesion. Consider a simple case of two arbitrarily positioned nanofibers collapsing due to surface adhesion as shown in figure 19. To simplify the process, the two fibers are assumed to carry the same fiber diameter, length and surface properties.

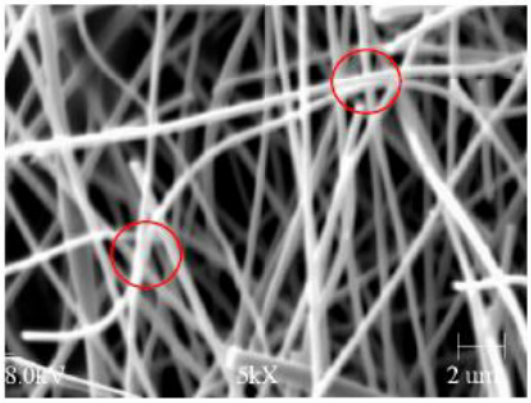

Figure 18. Adhesion between nanofibers within a PAN nanofiber network (Nanofiber diameter: ~300 nm, circles indicate the adhesion zones) [125]. Copyright (2007) of the Institute of Physics.

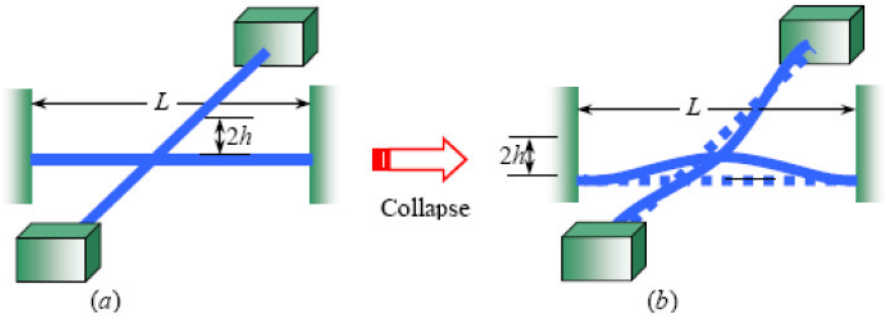

Figure 19. Adhesion between two nanofiber segmentspositioned in an arbitrary angle [125]. Copyright (2007) of the Institute of Physics.

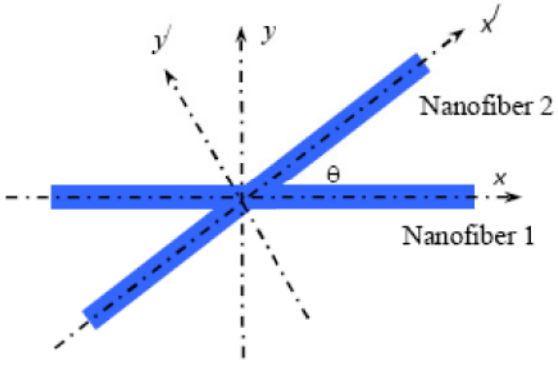

Figure 20. Geometries of two fibers positioned at an arbitrary angle θ.

Consider two uniform fiber segments positioned in two parallel horizontal planes with a distance h. The spatial angle between the fiber axes is denoted as θ. Simple relationships can be established between two coordinate systems attached to the fiber axes as shown in figure 20:

$$\begin{cases} x' = x\cos\theta + y\sin\theta, \\ y' = -x\sin\theta + y\cos\theta. \end{cases} \tag{26}$$

After fiber collapse due to surface adhesion as shown in figure 19(*b*), the asymptotic distance between two points on the surfaces of deflected fiber segments near the contact point is [125]

$$\begin{aligned} z &= 3h[(\frac{2x}{L})^2 - \frac{2}{3}(\frac{2x}{L})^3] + \frac{y^2}{2r} + 3h[(\frac{2x'}{L})^2 - \frac{2}{3}(\frac{2x'}{L})^3] + \frac{y'^2}{2r} + h_0 \\ &\approx \frac{12h}{L^2}x^2 + \frac{y^2}{2r} + \frac{12h}{L^2}x'^2 + \frac{y'^2}{2r} + h_0 \\ &\approx \frac{12h}{L^2}[(1+\cos^2\theta)x^2 + \sin 2\theta xy + \sin^2\theta y^2] \\ &\quad + \frac{1}{2r}[\sin^2\theta x^2 - \sin 2\theta xy + (1+\cos^2\theta)y^2] + h_0, (\text{for } x/L << 1 \text{ and } x'/L << 1) \end{aligned} \tag{27}$$

where local coordinates have been used. By using Bradley's approach [160], integrating relation (18) over the area out of the contact zone yieldsthe adhesive force between the two fibers:

$$\begin{aligned} P &= \int_\Gamma \sigma(z)dA = \frac{8\Delta\gamma}{3\varepsilon}\int_{-\infty}^{+\infty}\int_{-\infty}^{+\infty}[(\frac{\varepsilon}{z})^3 - (\frac{\varepsilon}{z})^9]dxdy, \\ &= \pi\Delta\gamma L/\sqrt{D}, \end{aligned} \tag{28}$$

where D is the determinant of a positive definite 2×2 matrix relating the fiber aspect ratio L/r, fiber distance h_c, and angle between fibers θ, i.e.

$$D = \begin{vmatrix} (1+\cos^2\theta)\frac{12h}{L} + \sin^2\theta\frac{L}{2r} & \sin\theta\cos\theta(\frac{12h}{L} + \frac{L}{2r}) \\ \sin\theta\cos\theta(\frac{12h}{L} + \frac{L}{2r}) & \sin^2\theta\frac{12h}{L} + (1+\cos^2\theta)\frac{L}{2r} \end{vmatrix}. \tag{29}$$

Substitution of (28) into the deflection formula of the nanofiber segment fixed at two ends and with a midspan deflection h: $P = 48\pi Er^4 h/L^3$ leads to the critical condition for nanofiber collapse as

$$\frac{h_c}{L} = \frac{1}{48\sqrt{D}}\frac{\Delta\gamma}{Er}(\frac{L}{r})^3. \tag{30}$$

With Dupré adhesion energy $\Delta\gamma=2\gamma$ for two equivalent nanofiber segments, relation (30) can be rewritten as

$$\frac{h_c}{L}=\frac{1}{24\sqrt{D}}\frac{\gamma}{Er}(\frac{L}{r})^3. \tag{31}$$

Furthermore, in the special cases of $\theta = 0^o$ and $\theta = 90^o$, the corresponding collapse conditions are respectively

$$(\frac{h_c}{L})^{3/2}=\frac{1}{48\sqrt{6}}\frac{\gamma}{Er}(\frac{L}{r})^{5/2}, \tag{32}$$

and

$$\frac{h_c}{L}=\frac{1}{12}(\frac{L}{r})^4\frac{\gamma}{Er}. \tag{33}$$

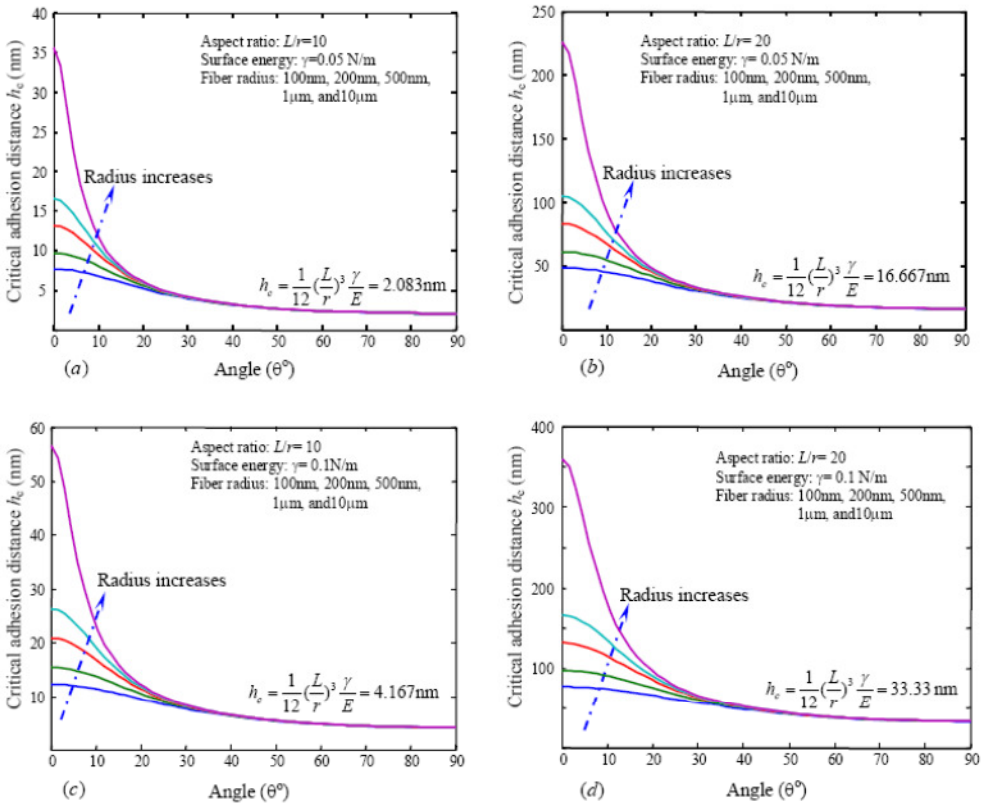

Figure 21. Variation of the critical collapse distance h_c between fiber segments vs. the nanofiber orientation angle θ at varying fiber radius r and aspect ratio L/r: (*a*) L/r = 10, γ = 0.05 N/m; (*b*) L/r = 20, γ = 0.05 N/m; (*c*) L/r = 10, γ = 0.1 N/m; and (*d*) L/r = 20, γ = 0.1 N/m [125]. Copyright (2007) of the Institute of Physics.

The general collapse criterion (31) involves the intrinsic length $l_0 = \gamma/E$, thus the following conclusion can be drawn that size effect does exist to govern the nanofiber collapse. For the convenience of discussion, relation (31) can be further cast into

$$\frac{h_c}{r} = \frac{1}{24\sqrt{D}} \frac{\gamma}{Er} \left(\frac{L}{r}\right)^4. \tag{34}$$

Numerical results on the dependency of the critical collapse distance upon the surface energy (surface tension) γ, fiber radius r are plotted in figure 21. During the numerical process, the surface energies of the fiberare selected as $\gamma = 0.05$ N/m and $\gamma = 0.1$ N/m, respectively; the Young's modulus is chosen as $E = 2$ GPa [125]. The numerical results shown in figure 21 clearly indicate thesize effect. Given a fiber pair, the critical collapse distance h_c decreases rapidly with increasing angle θ; meanwhile the critical collapse distance decreases with increasing surface energy. In addition, given an aspect ratio of the fiber segment L/r, at a small angle θ, h_c increases with the increase of fiber radius; however, at a relatively large angle θ, h_c tends to a constant, i.e., $(1/12)(L/r)^3\gamma/E$. This constant depends only upon the aspect ratio L/r and the intrinsic length $\gamma/E = 0.025$ nm for $\gamma = 0.05$ N/m, and $\gamma/E = 0.05$ nm for $\gamma = 0.1$ N/m. This parameter is expected to be useful for collapse analysis and reliable design of nanofiber networks as well as nanofiber devices. In addition, at a given fiber radius, h_c grows abruptly with the increase of L/r. Such effect can be interpreted in the sense of variation of the bending stiffness of a fiber segment which rapidly decreases with increasing fiber segment length based on a reciprocal cubic law.

3. Axial Deformation, Wave Propagation and Surface Rippling in Polymer Nanofibers [122, 123,126]

As discussed in the above, continuous nanofibers produced by electrospinning represent a new class of 1D nanomaterials. Their continuity, high surface area to volume ratio, and tailorable diameter (1-2,000 nm), surface morphology and microstructures make electrospun nanofibers numerous innovative applications in nanocomposites, filtration, protective clothing, biomedical engineering and technologies, nanodevices, etc. [7-17]. The mechanical behaviors of nanofibers are fundamental to their broad applications. In this section, simple 1D nonlinear continuum mechanics models [122, 123, 126] developed recently by the first author and his co-workers are reviewed; these models have taken into account the combined effect of surface energy and nonlinear elasticity in the mechanical responses (e.g., deformation, wave propagation, and surface rippling, etc.) of compliant polymer nanofibers. These models are capable of interpreting a series of size-related mechanical phenomena as observed in polymer nanofibers, and can also predict new surface stability conditions useful to nanofiber fabrication.

3.1. Static Tensile Deformation Subjected to Axial Stretching [123]

Consider a compliant polymer nanofiber as a circular cylinder at stretch-free state. Two configurations are adopted to describe the motion of a material point of the fiber, i.e., the

stretch-free configuration (with surface tension ignored) and the current configuration subjected to a finite axial stretch. The corresponding coordinates of the material point are denoted by (R, Θ, Z) and (r, θ, z), respectively. Subjected to uniform axial stretching, the axisymmetric deformation can be described as:

$$r = \lambda_1 R \ (0 \le R \le R_0), \qquad \theta = \Theta \ (0 \le \Theta \le 2\pi),$$
$$z = \lambda_3 Z \ (-\infty \le Z \le +\infty), \tag{35}$$

where R_0 is the initial radius of the stretch-free nanofiber (with surface-tension ignored), and λ_1 and λ_3 are the transverse and longitudinal stretches, respectively.

The constitutive law of the polymer nanofibers is modeled to follow that of isotropically, incompressible hyperelastic Mooney-Rivlin solid [161], which can be expressed as the Cauchy stress tensor **T** vs. the left Cauchy-Green tensor **B** corresponding to deformation (35):

$$\mathrm{T} = -p\mathrm{I} + 2c_1\mathrm{B} - 2c_2\mathrm{B}^{-1}, \tag{36}$$

where p is the hydrostatic pressure, and c_1 and c_2 are two material constants. The stress equilibrium equations are:

$$\partial T_{rr} / \partial r + (T_{rr} - T_{\theta\theta}) / r = 0, \tag{37}$$

$$\partial T_{\theta\theta} / \partial \theta = 0, \tag{38}$$

$$\partial T_{zz} / \partial z = 0. \tag{39}$$

Two traction boundary conditions (BCs) on the fiber surface and along the axial direction are evoked:

$$T_{rr} = -\gamma / r_0 \ \ (r = r_0), \tag{40}$$

$$P = 2\pi \int_0^{r_0} r T_{zz} dr + 2\pi r_0 \gamma. \tag{41}$$

In the above, γ (N/m) is the surface energy of the amorphous polymer fiber which is assumed being independent of the current fiber radius r_0 or the applied axial stretch λ_3, and P is the axial tensile force. Solving (37-39) under BCs in (40) and (41) yields [123]

$$P = 2\pi R_0^2 (\lambda_3 - \lambda_3^{-2})(c_1 - c_2 \lambda_3^{-1}) + \pi R_0 \gamma \lambda_3^{-1/2}, \tag{42}$$

which shows the surface/size effect in the axial deformation.

3.2. Longitudinal Wave Propagation in Pre-Stretched Nanofibers [126]

When considering longitudinal wave propagation in a pre-stretched polymer nanofiber, the dynamic motion is treated as a small disturbance superimposed on the axisymmetric deformation of the nanofiber given in (35). The perturbed state is described by coordinates ($\tilde{r}$, $\tilde{\theta}$, $\tilde{z}$). Thus, for a small disturbance, coordinates of a material point in the perturbed configuration can be described as

$$\tilde{r} = [\lambda_1 + f(Z,t)]R, \quad \tilde{\theta} = \Theta, \quad \tilde{z} = \lambda_3 Z + g(Z,t), \tag{43}$$

where $f(Z, t)$ and $g(Z, t)$ are two small time-dependent disturbance functions satisfying BCs in (40) and (41).

The governing wave propagation equation can be derived by using the principle of least action (Hamilton's law):

$$\delta \int_{t_1}^{t_2} L dt = 0, \tag{44}$$

where

$$L = T - \Pi. \tag{45}$$

In the above, t_1 and t_2 are two arbitrary starting and ending times, L is the modified lagrangian, and T and Π are respectively the kinetic energy and potential energy of the nanofiber segment under consideration which are defined as [126]

$$T = 1/4\pi R_0^4 \int_{L_0} \rho \dot{f}^2 dZ + 1/2\pi R_0^2 \int_{L_0} \rho \dot{g}^2 dZ, \tag{46}$$

$$\Pi = 2\pi \int_L \int_0^{R_0} eRdRdZ + 2\pi R_0 \gamma \int_{L_0} (\lambda_1 + f)(\lambda_3 + g_z) dZ - P \int_{L_0} (\lambda_3 + g_z - 1) dZ, \tag{47}$$

in which $\dot{f}$ and are respectively the transverse deformation rate (strain rate) and the axial translational speed of a material point, and ρ is the mass density, e is the strain energy density of incompressible hyperelastic Mooney-Rivlin solid defined by [161]

$$e = c_1(I_1 - 3) + c_2(I_2 - 3), \tag{48}$$

with I_1 and I_2 respectively the first and second invariants of the left Cauchy-Green tensor of perturbed deformations given in (43). The three terms in (47) are the contributions due to elastic strain energy, surface energy, and mechanical work done by the axial force P, respectively. In addition, the integration with respect to Z runs over the entire length L_0 of the fiber segment under consideration.

After several variational operations and eliminating the higher order terms based on small perturbation assumption, the necessary condition for an extremum of functional in (44) leads to a linearized longitudinal wave propagation equation:

$$R_0^2\rho\ddot{g}_{ZZ} - 8\lambda_3^3\rho\ddot{g} - 2(c_1 + c_2\lambda_3^{-1})R_0^2 g_{ZZZZ} + 8(4c_1 + 2c_1\lambda_3^3 + 6c_2\lambda_3^{-1} - \gamma/(2R_0)\lambda_3^{1.5})g_{ZZ} = 0. \tag{49}$$

To determine the wave dispersion relation, assume the travelling longitudinal wave to carry the mode:

$$g(Z,t) = A_0 \exp[ik(Z - ct)], \tag{50}$$

where A_0 is the complex amplitude of the wave disturbance, k is the wave number, and c is the wave phase speed. Substituting (50) into (49) results into the wave dispersion relation:

$$Ak^2c^2 + Bc^2 - Ck^2 - D = 0, \tag{51}$$

where

$$A = R_0^2\rho,\ B = 8\lambda_3^3\rho,\ C = 2(c_1 + c_2\lambda_3^{-1})R_0^2, \tag{52}$$

$$D = 8[4c_1 + 2c_1\lambda_3^3 + 6c_2\lambda_3^{-1} - \gamma/(2R_0)\lambda_3^{1.5}]. \tag{53}$$

By introducing the intrinsic length l_0 [123] and reference wave phase speed c_0 of the polymer material:

$$l_0 = \gamma/c_1,\ c_0 = \sqrt{c_1/\rho}, \tag{54}$$

Relation (51) can be recast as

$$(\frac{c}{c_0})^2 = \frac{2[1+(c_2/c_1)\lambda_3^{-1}]k_0^2 + 8[4 + 2\lambda_3^3 + 6(c_2/c_1)\lambda_3^{-1} - 0.5(l_0/R_0)\lambda_3^{1.5}]}{k_0^2 + 8\lambda_3^3}. \tag{55}$$

In the above, if ignoring the transverse motion of the nanofiber in (49), the wave speed can be determined from (55) as

$$(c/c_0)^2 = 4\lambda_3^{-3} + 2 + 6(c_2/c_1)\lambda_3^{-4} - 0.5(l_0/R_0)\lambda_3^{-1.5}. \tag{56}$$

In addition, in the limiting case of wave propagation in a stretch-free nanofiber (λ_3=1), i.e., an infinitesimal deformation, relation (56) can be reducedinto

$$c = \sqrt{E_T/\rho - \gamma/(2\rho R_0)}, \tag{57}$$

where E_T is the tangential modulus of hyperelastic Mooney-Rivlin solid at $\lambda_3 = 1$:

$$E_T = 6(c_1 + c_2). \tag{58}$$

Relation (57) covers the case of longitudinal waves propagating in linearly elastic nanowires (with Poisson's ratio $\upsilon = 0.5$) [122].

3.3. Surface Rippling of Nanofibers Subjected to Axial Pre-Stretch [126]

The governing equation of longitudinal wave propagation (49) can be utilized for the study of surface rippling phenomenon as observed recently in compliant as-electrospun PAN nanofibers subjected to axial stretching [126, 144, 145, 150]. Governing equation of surface rippling in polymer nanofibers can be obtained by eliminating the two inertia terms in Eq. (49) such that

$$Cg_{ZZZZ} - Dg_{ZZ} = 0, \tag{59}$$

where C and D are defined in (52) and (53). The ripple wave number k can be determined by assuming the rippling modes in the form:

$$g(Z) = B_0 \exp(ikZ), \tag{60}$$

where B_0 is the complex amplitude of wave disturbance similar to that in (50). Substitutionof (60) into (59) results in the ripple wave number:

$$k^2 = -D / C. \tag{61}$$

For physically meaningful rippling mode, k must be a positive number. This condition implies that surface rippling happens only under the condition $D < 0$.

Based on relation (53), the critical condition to trigger surface rippling in compliant nanofibers can be determined as

$$R_0 < (l_0 / 4) / [2\lambda_3^{-1.5} + \lambda_3^{1.5} + 3(c_2 / c_1)\lambda_3^{-2.5}]. \tag{62}$$

Relation (62) can be further used to determine an important geometrical parameter in nanofiber fabrication, i.e., the minimum critical fiber radius $(R_C)_{min}$, below which surface rippling can even happen spontaneously without any pre-stretch (i.e., $\lambda_3 = 1$). By setting λ_3=1 in relation (62), it leads to

$$(R_C)_{min} = \gamma / (2E_T) = (\gamma / 12) / (c_1 + c_2). \tag{63}$$

For typical rubbery polymer nanofibers, relation (63) determines that $(R_C)_{min}$≈10-40 nm. In principle, below $(R_C)_{min}$, compliant nanofibers cannot exist due to their spontaneous

surface destabilization (rippling). This indicates that it is physically impossible to fabricate compliant nanofibers with the fiber radius below $(R_C)_{min}$. Detailed discussions on surface rippling in polymer nanofibers are available elsewhere [126]. In summary, the above 1D nonlinear continuum mechanics models can be utilized to clarify the dependencies of axial deformation, longitudinal wave dispersion, and surface rippling condition in compliant polymer nanofibers upon the surface energy, nonlinear elastic properties, and fiber diameter. These results can be considered as the theoretical basis of manufacturing, static and dynamic characterization of compliant nanowires/nanofibers, nanofiber device design, etc.

3.4. Hydroelastic Response of Nanofibers [129]

In Section 3.3, 1D continuum mechanics models have been discussed to understand the mechanical behavior of nanofibers. In reality, a significant number of polymers work in aqueous environments such as human body wound dressing, in-plants, liquid filters, etc. In such cases, moisture and liquids may alter the mechanical behavior of these polymers, especially in the case of ultrathin fibers where the capillary force would be significant. Here introduce our recent study on the axial mechanical response of an ultrathin polymer fiber wetted with droplets and subjected to axial stretch as shown in figure 22 [129]. The polymer fiber is modeled as an incompressible, isotropic, hyperelastic Mooney-Rivlin solid [161] that can be expressed in terms of Cauchy stress tensor **T** vs. the left Cauchy-Green tensor **B** as shown in Eq. (36). Similar to those discussed in Section 3.3, the nanofiber is treated as an ultrathin circular cylinder of initial radius R_0. Two configurations are introduced to describe the deformation of the fiber, i.e., undisturbed stretch-free (without droplet and fiber surface stress) with coordinates (R, Φ, Z) and current configuration (after deformation under the capillary force and stretch) with coordinates (r, φ, z), respectively. We only consider the deformation of the fiber within the droplet and avoid the complicated phenomena near the wetting fronts.

The governing equations of the fiber are the same as Eqs. (37-39), while two traction BCs involving capillary effect are triggered. At the fiber surface, both interface tension and capillary effect yield uniform radial compression:

$$T_{rr} = -\gamma_{LS} / r_0 - p_c + 2\gamma_{LV} \sin\theta / L. \tag{64}$$

In the above, the first term is the compressive stress due to the specific interface energy γ_{LS} (N/m) which is assumed to be independent of the radius and the fiber axial stretch λ_3; and r_0 is the current radius; the second term is the capillary pressure p_c due to the droplet that can be determined by solving the Young-Laplace equation; the third term is the capillary forces at the two wetting fronts by averaging over the wetting length. In the axial direction, force equilibrium reads [129]

$$P = 2\pi \int_0^{r_0} r T_{zz} dr + 2\pi r_0 \gamma_{LV} \cos\theta, \tag{65}$$

where P is the axial tensile force required to maintain the axial equilibrium. Solving Eqs. (37-39) under BCs (64) and (65) with the aid of the available solution of a droplet wetting a fiber

[162,163] yields the relationship between the engineering stress σ of the fiber within the droplet and the axial stretch λ_3 [129]:

$$\sigma = \frac{P}{\pi R_0^2} = 2(\lambda_3 - \frac{1}{\lambda_3^2})(c_1 + \frac{c_2}{\lambda_3}) + \frac{2\gamma_{LV}\cos\theta - \gamma_{LV}}{\sqrt{\lambda_3} R_0} - \frac{p_c}{\lambda_3} + \frac{2\gamma_{LV}\sin\theta}{\lambda_3 L}. \tag{66}$$

In the above, p_c and L are respectively the capillary pressure and wetting length, which can be determined by solving the relevant Young-Laplace equation [162,163]. Numerical results of detailed scaling properties of relation (66) are plotted in figure 23 [129].

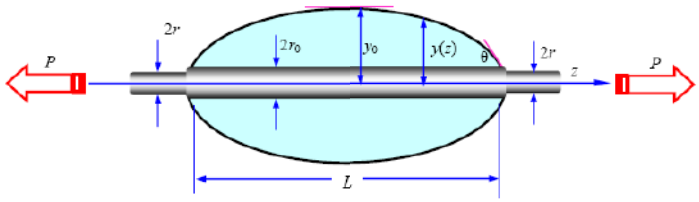

Figure 22. Geometries of a barrel-shaped droplet wetting on a thin compliant fiber subjected to axial stretch. In the diagram, r is the current fiber radius out of the droplet, and r_0 is the fiber radius within the droplet [129]. Copyright (2010) of the American Institute of Physics.

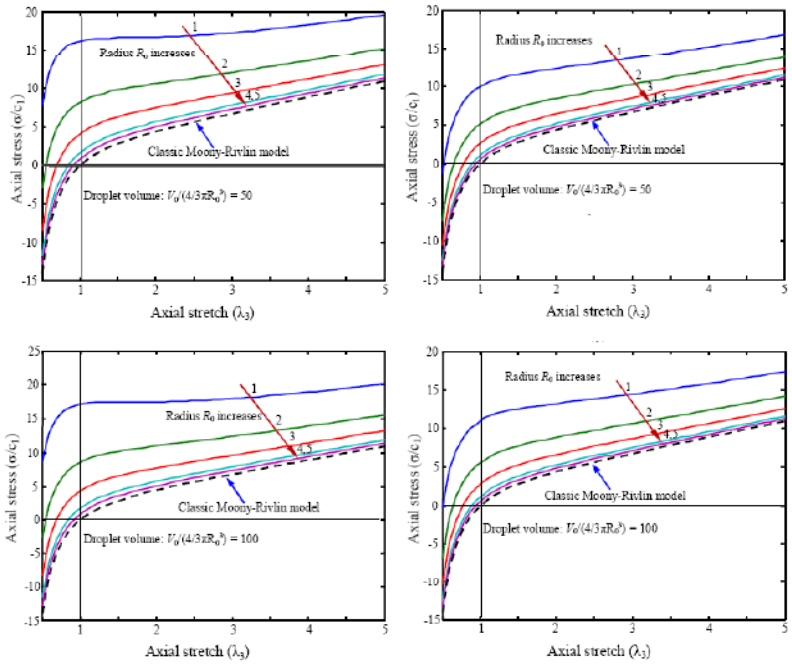

Figure 23. Comparison of the axial stress-stretch relationships of droplet-wetted rubbery fibers at varying initial fiber radius R_0, contact angle θ and droplet volume V_0 with that of classic Mooney-Rivlin model. In the diagrams, indices 1, 2, 3, 4 and 5 denote the fibers with initial radii 50 nm, 100 nm, 200 nm, 500 nm, and 1000 nm, respectively; the vertical line indicates the stretch-free state, i.e. $\lambda_3 = 1$ [129]. Copyright (2010) of the American Institute of Physics.

CONCLUDING REMARKS

In summary, in this chapter detailed review has been given to the production, mechanical characterization and mechanics modeling of continuous nanofibers by means of the novel, low-cost, top-down electrospinning technique. Several recently developed experimental techniques for nanofiber fabrication and mechanical characterization of continuous nanofibers are reviewed; the unique mechanical responses of electrospun nanofibers such as the size effect in the tensile mechanical behavior have been discussed. Several novel 1D continuum mechanics models have been discussed which can be utilized to correlate the experimental observations of electrospun nanofibers including the size effect in mechanical properties, wave propagation, surface rippling, adhesion and contact, surface wetting, and hydroelastic response, among others. These mechanics models are deemed useful to provide novel fundamental understanding of the principles for manufacturing and characterization of continuous electrospun nanofibers for a variety of applications.

ACKNOWLEDGMENT

Partial support of the research by the NSF, U.S. DOE EPSCoR-SUNRISE, ND NASA EPSCoR, ND Soybean Council, NDSU Development Foundation, and the Ashland Inc. (OH) is gratefully appreciated.

REFERENCES

[1] J. Doshi and D. H. Reneker, *J. Electrostatics* 35, 151 (1995).
[2] D. H. Reneker and I. Chun, *Nanotechnology* 7, 216 (1996).
[3] D. H. Reneker, A. L. Yarin, E. Zussman, and H. Xu, *Adv. Appl. Mech.* 41, 43 (2007).
[4] D. H. Reneker and A. L. Yarin, *Polymer* 49, 2387 (2008).
[5] Y. Dzenis, *Science* 304, 1917 (2004).
[6] D. Li and Y. N. Xia, *Adv. Mater.* (Weinheim, Ger.) 16, 1151 (2004).
[7] G. C. Rutledge and S. V. Fridrikh, *Adv. Drug Delivery Rev.* 59, 1384 (2007).
[8] Z. M. Huang, Y. Z. Zhang, M. Kotaki, and S. Ramakrishna, *Compos. Sci. Tech.* 63, 2223 (2003).
[9] A. Greiner and J. H. Wendorff, *Angew. Chem. Int. Ed.* 46, 5670 (2007).
[10] R. Ramaseshan, S. Sundarrajan, R. Jose, and S. Ramakrishna, *J. App. Phys.* 102, 111101 (2007).
[11] S. Ramakrishna, K. Fujihara, W. E. Teo, T. C. Lim, and Z. Ma, *An Introduction to Electrospinning and Nanofibers*, World Scientific, Singapore (2005).
[12] A. L. Andrady, *Science and Technology of Polymer Nanofibers*, Jon Wiley and Son (2008).
[13] Z. L. Wang (ed.), *Nanowires and Nanobelts: Materials, Properties and Devices*, volume 2: Nanowires and Nanobelts of Functional Materials, Springer, New York (2003).

[14] S. Guceri, Y. G. Gogotsi, and V. Kuznetsov (ed.), *Nanoengineered Nanofibrous Materials*, Kluwer Academic Publishers, Boston (2003).
[15] G. Cao, *Nanostructures and Nanomaterials: Synthesis, Properties and Applications*, Imperial College Press, London, U.K. (2004).
[16] I. S. Chronakis, *J. Mater. Processing. Tech.* 167, 283 (2005).
[17] A. Baji, Y. W. Mai, S. C. Wong, M. Abtahi, and P. Chen, *Compos. Sci. Tech.* 70, 703 (2010).
[18] G. Taylor, *Proc. Roy. Soc. Lond. A* 313, 453 (1969).
[19] A. F. Spivak and Y. A. Dzenis, *J. Appl. Mech.* 66, 1026 (1999).
[20] A. L. Yarin, S. Koombhongse, and D. H. Reneker, *J. Appl. Phys.* 89, 3018 (2001).
[21] C. Lai, Q. Guo, X. F. Wu, D. H. Reneker, and H. Hou, *Nanotechnology* 19, 195303 (2008).
[22] W. E. Teo and S. Ramakrishna, *Nanotechnology* 17, R89 (2006).
[23] P. Gibson, H. Schreuder-Gibson, and D. Rivin, *Colloids Surfaces A –Physicochem. Eng. Asp.* 187, 469 (2001).
[24] R. Gopal, S. Kaur, Z. W. Ma, C. Chan, S. Ramakrishna, and T. Matsuura, *J. Membrane Sci.* 281, 581 (2006).
[25] R. S. Barhate and S. Ramakrishna, *J. Membrane Sci.* 296, 1 (2007).
[26] B. Maze, H. V. Tafreshi, Q. Wang, and B. Pourdeyhimi, *J. Aerosol Sci.*38, 550 (2007).
[27] Y. M. Sang, Q. B. Gu, T. C. Sun, F. S. Li, and C. Z. Liang, *J. Hazardous M.* 153, 860 (2008).
[28] M. Bognitzki, H. Q. Hou, M. Ishaque, T. Frese, M. Hellwig, C. Schwarte, A. Schaper, J. H. Wendorff, and A. Greiner, *Adv. Mater.* 12, 637 (2000).
[29] W. X. Liu, M. Graham, E. A. Evans, and D. H. Reneker, *J. Mater. Res.* 17, 3206 (2002).
[30] J. Sutasinpromprae, S. Jitjaicham, M. Nithitanakul, C. Meechaisue, and P. Supaphol, *Polym. Int.* 55, 825 (2006).
[31] K. S. Yang, D. D. Edie, D. Y. Lim, Y. M. Kim, and Y. O. Choi, *Carbon* 41, 2039 (2003).
[32] J. S. Kim and D. H. Reneker, *Polym. Compos.* 20, 124 (1999).
[33] Y. Dzenis, *Science* 319, 419 (2008).
[34] X. F. Wu, *Fracture of Advanced Composites with Nanostructured Interfaces: Fabrication, Characterization and Modeling*, VDM Publishing House, Germany (2009).
[35] D. Smith, D. H. Reneker, W. Kataphinan, and A. Dabney, *US Patent* 6821479 (2001).
[36] D. Smith and D. H. Reneker, *US Patent* 6753454 (2004).
[37] W. J. Li, C. T. Laurencin, E. J. Caterson, R. S. Tuan, and F. K. Ko, *J. Biomed. Mater. Res.* 60, 613 (2002).
[38] J. A. Matthews, G. E. Wnek, D. G. Simpson, and G. L. Bowlin, *Biomacromolecules* 3, 232 (2002).
[39] C. Burger, B. S. Hsiao, and B. Chu, *Ann. Rev. Mater. Res.* 36, 333 (2006).
[40] Q. P. Pham, U. Sharma, and A. G. Mikos, *Tissue Eng.* 12, 1197 (2006).
[41] C. P. Barnes, S. A. Sell, E. D. Boland, D. G. Simpson, and G. L. Bowlin, *Adv. Drug Delivery Rev.* 59, 1413 (2007).
[42] J. Xie, X. Li, and Y. Xia, *Nature Mater.* 29, 1775 (2008).

[43] E. R. Kenawy, G. L. Bowlin, K. Mansfield, J. Layman, D. G. Simpson, E. H. Sanders, and G. E. Wnek, *J. Contr. Release* 81, 57 (2002).
[44] S. Y. Chew, Y. Wen, Y. Dzenis, and K. W. Leong, *Curr. Pharm. Design* 12, 4751(2006).
[45] D. Liang, B. S. Hsiao, and B. Chu, *Adv. Drug Delivery Rev.* 59, 1392 (2007).
[46] S. G. Kumbar, S. P. Nukavarapu, R. James, M. V. Hogan, and C. T. Laurencin, *Recent Patents Biomed. Eng.* 1, 68 (2008).
[47] K. Onozuka, B. Ding, Y. Tsuge, T. Naka, M. Yamazaki, S. Sugi, S. Ohno, M. Yoshikawa, and S. Shiratori, *Nanotechnology* 17, 1026 (2006).
[48] M. Y. Song, D. K. Kim, K. J. Ihn, S. M. Jo, and D. Y. Kim, *Nanotechnology* 15,1861 (2004).
[49] L. Jiang, Y. Zhao, and J. Zhai, *Ange. Chem. Int. Ed.* 43, 4438 (2004).
[50] Y. Miyauchi, B. Ding, and S. Shiratori,*Nanotechnology* 17, 5151 (2006).
[51] X. Y. Wang, C. Drew, S. H. Lee, K. J. Senecal, J. Kumar, and L. A. Samuelson, *J. Macromolecular Sci.* A39, 1251 (2002).
[52] B. Ding, J. H. Kim, Y. Miyazaki, and S. M. Shiratori, *Sensors and Actuators B-Chem.* 101, 373 (2004).
[53] D. Aussawasathien, J. H. Dong, and L. Dai, *Synthetic Metals* 154, 37 (2005).
[54] M. K. Tiwari, A. L. Yarin, and C. M. Megaridis, *J. Appl. Phys.* 103, 044305 (2008).
[55] B. Ding, M. Wang, J. Y. Yu, and G. Sun, *Sensors* 9, 1609 (2009).
[56] I. D. Norris, M. M. Shaker, F. K. Ko and A. G. MacDiarmid, *Synth. Metals* 114, 109 (2000).
[57] M. J. Laudenslager, R. H. Scheffler, and W. M. Sigmund, *Pure Appl. Chem.* 82, 2137 (2010).
[58] D. L. Schulz, J. Hoey, J. Smith, A. Elangovan, X. Wu, I. Akhatov, S. Payne, J. Moore, P. Boudjouk, L. Pederson, J. Xiao, and J. G. Zhang, *Electrochem. Solid-State Lett.* 13, A143 (2010).
[59] X. Zhang, L. Ji, O. Toprakci, Y. Liang, and M. Alcoutlabi, *Polym. Rev.* 51, 239 (2011).
[60] S. A. Theron, A. L. Yarin, E. Zussman, and E. Kroll, *Polymer* 46, 2889 (2005).
[61] A. L. Yarin and E. Zussman, *Polymer* 45, 2977 (2004).
[62] A. Sarkar and D. Lukas, *6th Int. Conf.-TEXSCI*, June 5-7, Czech Republic (2007).
[63] D. Lukas, A. Sarkar, and P. Pokorny, *J. Appl. Phys.* 103, 084309 (2008).
[64] D. Lukas, A. Sarkar, L. Martinova, K. Vodsed'alkova, D. Lubasova, J. Chaloupek, P. Pokorny, P. Mikes, J. Chvojka, and M. Komarek, *Textile Progress* 41, 59 (2009).
[65] S. Petrick and M. Maly, *Production of Nozzleless Electrospinning Nanofiber Technology* (Presentation), Liberc, Czech Republic (2009).
[66] Z. Sun, E. Zussman, A. Yarin, and J. H. Wendorff, and A. Greiner, *Adv. Mater.* 15, 1929 (2003).
[67] D. Li and Y. N. Xia, *Nano Lett.* 4, 933 (2004).
[68] D. Li, A. Babel, S. A. Jenekhe, and Y. N. Xia, *Adv. Mater.* 16, 2062 (2004).
[69] A. V. Bazilevsky, A. L. Yarin, and C. M. Megaridis, *Langmuir* 23, 2311 (2007).
[70] Y. Dror, W. Salalha, R. Avrahami, E. Zussman, A. L. Yarin, R. Dersch, A. Greiner, and J. H. Wendorff, *Small* 3 1064 (2007).
[71] A. L. Yarin, E. Zussman, J. H. Wendorff, and A. Greiner, *J. Mater. Chem.* 17, 2585 (2007).
[72] A. L. Yarin, *Polym. Adv. Tech.* 22, 310 (2011).

[73] T. Miloh, B. Spivak, and A. L. Yarin, *J. Appl. Phys.*106, 114910 (2009).
[74] X. F. Wu and Y. A. Dzenis, *J. Phys. D. Appl. Phys.* 38, 2848 (2005).
[75] L. D. Landau and E. M. Lifshitz, *Fluid Mechanics* (2nd Ed.), Oxford: Butterworth-Heinemann (1987).
[76] E. Schaffer, T. Thurn-Albrecht, T. P. Russell, and U. Steiner, *Nature* 403, 874 (2000).
[77] E. Schaffer, T. Thurn-Albrecht, T. P. Russell, and U. Steiner, *Europhys. Lett.* 53, 518 (2001).
[78] L. F. Pease and W. B. Russel, *J. Non-Newtonian Fluid Mech.* 102, 233 (2002).
[79] L. Wu and S. Y. Chou, *Appl. Phys. Lett.* 82, 3200 (2003).
[80] L. Wu and S. Y. Chou, *J. Non-Newtonian Fluid Mech.* 125, 91 (2005).
[81] R. Verma, A. Sharma, K. Kargupta, and J. Bhaumik, *Langmuir* 21, 3710 (2005).
[82] N. Wu, L. F. Pease, and W. B. Russel, *Langmuir* 21, 12290 (2005).
[83] N. Wu, L. F. III Pease, and W. B. Russel, *Adv. Functional Mater.* 16, 1992 (2006).
[84] D. Kim and W. Lu, *Phys. Rev. E* 73, 035206 (2006).
[85] S. Srivastava, P. D. S. Reddy, C. Wang, D. Bandyopadhyay, and A. Sharma, *J. Chem. Phys.* 132, 174703 (2010).
[86] V. G. Suvorov and E. A. Litvinov, *J. Phys. D: Appl. Phys.* 33, 1245 (2000).
[87] S. N. Reznik, A. L. Yarin, A. Theron, and E. Zussman, *J. Fluid Mech.* 516, 349 (2004).
[88] V. N. Kirichenko, I. V. Petryanov-Sokolov, N. N. Suprun, and A. A. Shutov, *Sov. Phys. Dokl.* 31, 611 (1986).
[89] A. F. Spivak and Y. A. Dzenis, *Appl. Phys. Lett.* 73, 3067 (1998).
[90] A. F. Spivak, Y. A. Dzenis, and D. H. Reneker, *Mech. Res. Comm.* 27, 37 (2000).
[91] M. M. Hohman, M. Shin, G. Rutledge, and M. P. Brenner, *Phys. Fluids* 13, 2201 (2001).
[92] M. M. Hohman, M. Shin, G. Rutledge, and M. P. Brenner, *Phys. Fluids* 13, 2221 (2001).
[93] Y. M. Shin, M. M. Hohman, M. P. Brenner, and G. C. Rutledge, *Appl. Phys. Lett.* 78, 1149 (2001).
[94] S. V. Fridrikh, J. H. Yu, M. P. Brenner, and G. C. Rutledge, *Phys. Rev. Lett.* 90, 144502 (2003).
[95] J. J. Feng, *Phys. Fluids* 14, 3912 (2002).
[96] J. J. Feng, *J. Non-Newtonian Fluid Mech.* 116, 55 (2003).
[97] I. Hayati, *Colloids Surface* 65, 77 (1992).
[98] F. J. Higuera, *J. Fluid Mech.* 484, 303 (2003).
[99] F. Yan, B. Farouk, and F. Ko, *Aerosol. Sci.* 34, 99 (2003).
[100] D. H. Reneker, A. L. Yarin, H. Fong, and S. Koombhongse, *J. Appl. Phys.* 87, 4531 (2000).
[101] A. L. Yarin, S. Koombhongse, and D. H. Reneker, *J. Appl. Phys.* 89, 3018 (2001).
[102] S. A. Theron, E. Zussman, and A. L. Yarin, *Polymer* 45, 2017 (2004).
[103] C. J. Thompson, G. G. Chase, A. L. Yarin, and D. H. Reneker, *Polymer* 48, 6913 (2007).
[104] Z. P. Zhou, X. F. Wu, X.Q. Gao, L. Jiang, Y. Zhao, and H. Fong, *J. Phys. D: Appl. Phys.* 44, 435401 (2011).
[105] P. Dayal and T. Kyu, *Phys. Fluids* 19, 107106 (2007).
[106] P. Dayal, J. Liu, S. Kumar, and T. Kyu, *Macromolecules* 40, 7689 (2007).
[107] X. F. Wu, Y. Salkovskiy, and Y. A. Dzenis, *Appl. Phys. Lett.,* 98, 223108 (2011).

[108] R. Saure, G. R. Wagner, and E. U. Schlunder, *Surface Coatings Tech.* 99 253 (1998).
[109] R. Saure, G. R. Wagner, and E. U. Schlunder, *Surface Coatings Tech.* 99, 257 (1998).
[110] P. J. Flory, *Principles of Polymer Chemistry*, (Cornell University Press, Ithaca, 1953).
[111] G. M. Bristow and W. F. Watson, *Trans. Farady Soc.* 54, 1731 (1958).
[112] S. J. Farlow, *Partial Differential Equations for Scientists and Engineers*, Dover, New York (1993).
[113] J. L. Duda, J. S. Vrentas, S. T. Ju, and H. T. Liu, *AIChE J.* 28, 279(1982).
[114] J. M. Zielinski and J. L. Duda, *AIChE J.* 38, 405 (1992).
[115] J. Crank, *The Mathematics of Diffusion*, Oxford University Press, Oxford (1975).
[116] Y. A. Dzenis and Y. Wen, *Mater. Res. Soc. Symp.-Proc.* 702, 173 (2002).
[117] D. H. Reneker and H. Fong (editors), *Polymeric Nanofibers*, Washington, DC: American Chemical Society (2005).
[118] F. P. Incropera and D. P. DeWitt, *Fundamentals of Heat and Mass Transfer* (4th ed.), John Wiley and Sons, New York (1996).
[119] S. Koombhongse, W. Liu, and D. H. Reneker, *J. Polym. Sci. B: Polym. Phys.* 39, 2598 (2001).
[120] M. Bognitzki, W. Czado, T. Frese, A. Schaper, M. Hellwig, M. Steinhart, A. Greiner, and J. H. Wendorff, *Adv. Mater.* 13, 70 (2001).
[121] X. F. Wu and Y. A. Dzenis, *J. Appl. Phys.* 98, 093501 (2005).
[122] X. F. Wu and Y. A. Dzenis, *J. Appl. Phys.* 100, 124318 (2006).
[123] X. F. Wu and Y. A. Dzenis, *J. Appl. Phys.* 102, 044306 (2007).
[124] X. F. Wu and Y. A. Dzenis, *J. Phys. D: Appl. Phys.* 40, 4276 (2007).
[125] X. F. Wu and Y. A. Dzenis, *Nanotechnology* 18, 285702 (2007).
[126] X. F. Wu, Y.Y. Kostogorova-Beller, A.V. Goponenko, H.Q. Hou, and Y.A. Dzenis, *Phys. Rev. E* 78, 061804 (2008).
[127] X. F. Wu, *J. Appl. Phys.* 107, 013509 (2010).
[128] X. F. Wu, A. Bedarkar, and K.A. Vaynberg, *J. Colloid Interface Sci.* 341, 326 (2010).
[129] X. F. Wu, A. Bedarkar, and I. S. Akhatov, *J. Appl. Phys.* 108, 083518(2010).
[130] A. Bedarkar and X. F. Wu, *J. Appl. Phys.* 106, 113527 (2009).
[131] A. Bedarkar, X. F. Wu, and A. Vaynberg, *Appl. Surface Sci.* 256, 7260 (2010).
[132] F. Chen, X. W. Peng, T. T. Li, S. L. Chen, X. F. Wu, D. H. Reneker, and H. Q. Hou, *J. Phys. D: Appl. Phys.* 41, 025308 (2008).
[133] E. Zussman, D. Rittel, and A. L. Yarin, *Appl. Phys. Lett.* 82, 3958(2003).
[134] C. Y. Cheng, J. Chen, F. Chen, P. Hu, X. F. Wu, D. H. Reneker, and H. Q. Hou, *J. Appl. Polym. Sci*. 116, 1581 (2010).
[135] E. P. S. Tan and C. T. Lim, *Rev. Sci. Instrum.* 75, 2581 (2004).
[136] E. P. S. Tan and C. T. Lim. *Appl. Phys. Lett.* 84, 1603 (2004).
[137] E. P. S. Tan, S. Y. Ng, and C. T. Lim, *Biomater.* 26, 1453 (2005).
[138] E. P. S. Tan , C. N. Goh, C. H. Sow, and C. T. Lim, *Appl. Phys. Lett.* 86, 073115 (2005).
[139] E. P. S. Tan and C. T. Lim, *Compos. Sci. Tech.* 66, 1102 (2006).
[140] C. T. Lim, E. P. S. Tan, and S. Y. Ng, *Appl. Phys. Lett.*92, 141908 (2008).
[141] E. Zussman, M. Burman, A. L. Yarin, R. Khalfin, and Y. Cohen, *J. Polym. Sci. B: Polym. Phys.* 44, 1482 (2006).
[142] M. K. Shin, S. I. Kim, S. J. Kim, S. K. Kim, H. Lee, and G. M. Spinks, *Appl. Phys. Lett.* 89, 231929 (2006).

[143] P. A. Yuya, Y. K. Wen, J. A. Turner, Y. A. Dzenis, and Z. Li, *Appl. Phys. Lett.* 90, 111909 (2007).
[144] M. Naraghi, I. Chasiotis, H. Kahn, Y. K. Wen, and Y. Dzenis, *Appl. Phys. Lett.* 91, 151901 (2007).
[145] M. Naraghi, I. Chasiotis, H. Kahn, Y. Wen, and Y. Dzenis, *Rev. Sci. Instrum.* 78, 085108 (2007).
[146] B. A. Samuel, M. A. Haque, B. Yi, R. Rajagopalan, and H. C. Foley, *Nanotechnology* 18, 115704 (2007).
[147] A. Arinstein, M. Burman, O. Gendelman, and E. Zussman, *Nature Nanotechnology* 2, 59 (2007).
[148] D. Edmondson, N. Bhattarai, S. Jana, A. Kim, and M. Q. Zhang, *Appl. Phys. Lett.* 94, 103101 (2009).
[149] Y. S. Zhang, E. P. S. Tan, C. H. Sow, and C. T. Lim, *Nanomechanical Characterization of One-Dimensional Nanostructures*, pp. 105, in *Micro and Nano Mechanical Testing of Materials and Structures* (edited by F. Q. Yang and J. C. M. Li), Springer (2008).
[150] M. Naraghi and I. Chasiotis, *Mechanics of PAN Nanofibers* in *Major Accomplishments in Composite Materials and Sandwich Structures: An Anthology of ONR Sponsored Research* (edited by I. M. Daniel), pp. 757, Springer (2009).
[151] Y. Ji, B. Q. Li, S. R. Ge, J. C. Sokolov, and M. H. Rafailovich, *Langmuir* 22, 1321 (2006).
[152] B. D. Coleman, *Arch. Ration. Mech. Anal.* 83, 115 (1983).
[153] H. H. Dai and Z. Cai, *Acta Mech.* 139, 201 (2000).
[154] Y. B. Fu and R. W. Ogden, *Nonlinear Elasticity: Theory andApplications,* Cambridge University Press, Cambridge, U. K. (2001).
[155] B. V. Derjaguin, V. M. Muller, and V. P. Toporov, *J. Colloid Interface Sci.* 53, 314 (1975).
[156] K. L. Johnson, *Contact Mechanics*, Cambridge: Cambridge University Press (1985).
[157] S. Timoshenko and J. N. Goodier, *Theory of Elasticity* (2nd Ed.), New York: McGraw-Hill (1965).
[158] L. D. Landau and E. M. Lifshitz, *Theory of Elasticity* (3rd Ed.), London: Butterworth-Heinemann (1986).
[159] D. Maugis, *Contact, Adhesion and Rupture of Elastic Solids*, Heidelberg: Springer-Verlag (2000).
[160] R. S. Bradley, *Philo. Mag.*13, 853 (1932).
[161] S. C. Cowin and S. B. Doty, *Tissue Mechanics*, Springer, New York (2007).
[162] B. J. Carroll, *J. Colloid Interface Sci.* 57, 488 (1976).
[163] X. F. Wu, Y.A. Dzenis, *Acta Mech.* 185, 215(2006).